Materials Today Communications 57 (2026) 116533

Contents lists available at ScienceDirect

Materials Today Communications

journal homepage: www.elsevier.com/locate/mtcomm

Aspects of mesh sensitivity for phenomenological damage models using small solid and large shell elements

Lilia Schuster [a,*,1], Sebastian Münstermann [b]

[a] wbk Institute of Production Science, Karlsruhe Institute of Technology (KIT), Kaiserstr. 12, Karlsruhe 76131, Germany
[b] Institute of Metal Forming, RWTH Aachen University, Intzestr. 10, Aachen 52072, Germany

ARTICLE INFO

Keywords:
Finite element analysis
Mesh sensitivity
Regularization
Damage modeling
Shell elements
Crash modeling
Characteristic length

ABSTRACT

Application-oriented simulations, such as automotive crash simulations, often utilize large shell elements to optimize computational efficiency. This study applies the crack band approach typically used for concrete materials to steel sheets. The aim was to examine this regularization method for different stress states with plane stress shell elements to reduce mesh sensitivity, in respect to element size as well as to element shape. Finite element simulations of four specimens covering the lower and mid triaxiality range were performed with LS-Dyna using small solid elements and large shell elements. For each specimen, the results of a finite element simulation performed with large shell elements were compared with results of a block of solid elements of equal dimensions. Each finite element solver uses different shell formulations, which can influence the exact results of the simulation. Nonetheless, the comparison provides insights into the expected behavior compared to the behavior resulting from shell simulations. The guidelines developed in this study were tested numerically for a tensile test with a spot weld by comparing differently discretized meshes. The results show that the characteristic length determined by the crack band approach improves shell element simulations compared to the conventionally calculated characteristic length. This approach accommodates various aspect ratios and arbitrarily shaped shell elements.

1. Introduction

For the finite element analysis of large structures, such as aircrafts, ships or automobiles, the finite element models are often meshed with shell elements. For the model of a full vehicle analysis, shell elements with edge lengths of 2 or 3 mm are used at relevant crash impact areas. However, damage relevant material behavior is driven on a much smaller scale. Fracture and damage can only be adequately described using small solids. With careful calibration, reasonable results can be achieved with shell elements, but the results are notably size-dependent. Therefore, regularization methods for shell elements are needed to account for mesh size effects and material behavior in the localized zone that cannot be resolved by large shell elements.

Generally, the material behavior in the localized zone can be described by micromechanical or phenomenological damage models. By adequately describing the behavior in the localized zone, macroscopic behavior such as softening and fracture initiation are captured by finite element analysis. However, if the finite element analysis is performed with large elements, the results of the analysis vary with the element size.

Various approaches exist in literature to address mesh size effects of large shells. In cohesive zone modeling, the bulk behavior is captured in continuum elements and the damage processes are captured using cohesive zone elements at the interface between the continuum elements. To effectively use the cohesive zone framework for larger scales, modifications to the framework are required [1]. The shape, peak-load and cohesive energy of the traction-separation law, which governs the cohesive element model are all affected by the size of the element [2]. For large structures, the strength of the cohesive element can be scaled by the element length and number of elements along the interface [3]. Most cohesive zone models use the dissipated fracture energy per crack area as a reference to scale the model for larger element sizes [4,5]. Capturing information on thickness reduction in the cohesive element by using the property of volume incompressibility of metals [6] is another approach to account for mesh size effects.

The crack band approach is a computationally efficient approach to

* Corresponding author.
E-mail address: lilia.schuster@kit.edu (L. Schuster).
[1] 0000-0001-8089-4523

https://doi.org/10.1016/j.mtcomm.2026.116533
Received 24 May 2026; Received in revised form 26 October 2026; Accepted 29 October 2026
Available online 30 October 2026
2352-4928/© 2026 The Author(s). Published by Elsevier Ltd. This is an open access article under the CC BY license (http://creativecommons.org/licenses/by/4.0/).
Open access funding enabled and organized by Projekt DEAL.

avoid mesh size effects [7]. It uses the fact that the strain-softening damage process localizes into one layer of elements for larger elements. The model parameters that control softening behavior are modified so that the same energy is dissipated per unit area of the shell element as in the height of the physical fracture process zone. The crack band approach is often used in applications involving concrete and geomaterials [8,9].

Some authors have developed special damage models [10–12] or variational damage models to deal with mesh size effects [13], whereas others have modified existing failure criteria or phenomenological damage models [14–16]. To account for mesh size effects in phenomenological damage models, the fracture locus can be scaled depending on element size and triaxiality [15], or a stress concentration exponent for different element sizes and triaxialities can be used [16].

In the context of regularization, the element size is also referred to as the characteristic length. The characteristic length must be clearly defined to employ any of these regularization models. Most often, the characteristic length is defined as the square root of the element area, which is equal to the edge length of a perfectly square element. It can be shown that for arbitrarily shaped elements and arbitrary aspect ratios of the element edge lengths, this can lead to ill-fitting regularization. This can be addressed by using other definitions of the characteristic length [17–19]. These methods build on earlier work, where it was suggested to calculate the characteristic length as a function of fracture energy [20].

Many regularization methods have been developed either for crack propagation in concrete structures or for modeling ship collisions. These applications either require a plane strain condition or deal with relatively large shell thicknesses of about 10 mm and often exhibit stress conditions with high triaxialities. Therefore, they are often unsuitable for applications in crash modeling, where sheet thicknesses are usually smaller than 3 mm and stress triaxialities can be on the lower side. How to deal with arbitrarily shaped elements and define the characteristic length, when the stress state varies remains an open question. Calibrating and validating these regularization models can be difficult, particularly when dealing with various stress triaxialities. The calibration tests must cover various stress states in shear, uniaxial, and biaxial loading, where the stress state must remain constant throughout the specimen loading. Calibration specimens often have details much smaller than the targeted shell element size for the analysis of large structures.

In this study, specimens for four stress states were calibrated using large shell elements and small solids. A comparison of the results of the shell and solid models provides a deeper understanding of the relationship between the effects of mesh size and triaxiality. The results indicate that elements with large aspect ratios do not necessarily negatively affect the simulation results. By strategically placing elements with large aspect ratios, negative effects caused by small geometric details can be avoided. The results also show that displacement is a better indicator for regularization, which is consistent with earlier studies on mesh sensitivity and regularization methods [20]. The simple shear specimens show that no regularization is required for a stress triaxiality of zero. While this is a known issue, an additional specimen that combines simple shear with uniaxial tension shows that tying regularization to the triaxiality may be insufficient, since triaxiality does not distinguish cases that combine simple shear and coaxial stretch from cases of only coaxial stretch [21–24].

This study provides guidelines for the calibration of shell elements for finite element analysis and the development of regularization methods. Guidelines to account for different element sizes in damage modeling that can be combined with any phenomenological damage model are presented. The exact results and implementation will vary depending on the shell element formulations. In the last section, aspects of the presented guidelines are tested on a practical example, where the deformation and failure of a softened heat-affected zone around a spot weld in a steel sheet under quasi-static loading are analyzed. The analysis relies on numerical simulation only and is not based on experimental results. The results suggest that by applying these guidelines, the effects of element size and aspect ratio can be reduced.

2. Material & methods

In this section, the experimental tests for the characterization resulting from press-hardening steel sheet material are described. The steel sheet used in this study was primarily designed for automotive structures. It is particularly relevant for the construction of the passenger cabins, such as the B-pillar, because it has a high ultimate tensile strength of approximately 2 GPa. The chemical composition of the material is described in Table 1. The steel sheet has a thickness of 1.0 mm and is coated with aluminium-silicone (AlSi). Due to the coating, which accounts for 0.1 mm on each side of the steel sheet, the Young's modulus is lowered in comparison to steel which has a Young's modulus of 210 GPa to a value of 182 GPa. This value was approximated by weighing the Young's modulus of steel (210 GPa) and aluminium (~69–71 GPa) according to the ratio of total thickness and coating thickness of the steel sheet. The simulation of the material behavior with this adjusted Young's modulus gives a good agreement with the experimental behavior in the elastic zone which we will see in more detail in Section 3.

Press-hardened steels are special in that they form a softened zone around the spot weld due to the heat treatment and recrystallization that occurs [25–27]. The characteristic mechanical properties of this heat-treated material and the base material are listed in Table 2. The first line describes the properties of the base material, which is the steel sheet in its fully press-hardened state. The second line describes the material properties, which occur after spot welding around the spot weld. This region is referred to as the softened heat-affected zone (SHAZ). Other names such as sub-critical heat affected zone are also common in literature.

For the microstructures similar to the SHAZ, the approach described in [25] was adopted. Strips of press-hardened steel were heat-treated in a Gleeble simulator to create microstructures similar to those of the material occurring in the spot weld. To obtain a microstructure similar to that of the SHAZ, a maximum temperature of 700 °C was used. This peak temperature was reached after 1.6 s, and the metal strips were then cooled at a rate of 190 K s-1. After heat treatment, specimens with the final geometry were extracted and tested. Flat tensile specimens for the base material (BM) were extracted from a fully press-hardened sheet.

2.1. Experimental procedures

For modeling of the ductility and the damage behavior, different stress states need to be considered. Four specimen geometries were tested and extracted from the heat-treated material strips by waterjet cutting. The dimensions of the specimens are shown in Fig. 1. These specimens will be referred to as uniaxial tensile test (ut) and notched tensile test (ntR4), shear test 45° (sh45) and shear test 0° (sh0). These tests cover a theoretical range of 0–0.57 for triaxiality. The uniaxial tensile test is designed to test a stress state of Lode parameter $\boldsymbol{\xi = 1}$ and triaxiality $\boldsymbol{\eta = \frac{1}{3}}$, the notched tensile test is designed to test plane strain with $\boldsymbol{\xi = 0}$ and $\boldsymbol{\eta = \frac{1}{\sqrt{3}}}$, the shear test 0° is designed to test simple shear with $\boldsymbol{\xi = 0}$ and $\boldsymbol{\eta = 0}$ and the shear test 45° falls in the range between simple shear and uniaxial tension.

The boundary conditions of the shear test 45° approximately agree with the load case discussed in [28]. For a unit cube tilted by an angle $\boldsymbol{\phi}$ from the horizontal axis and pulled in the vertical direction, where the upper plane of the cube has two translational degrees of freedom, the triaxiality can be calculated using Equation (1).

$$\boldsymbol{\eta = \left(\sqrt{3}\sqrt{1 + 4 \cdot \tan^2 \phi}\right)^{-1}} \tag{1}$$

Table 1
Chemical compositions of steels, mass content in 0.001 wt%.

Material[a])	C	Si	Mn	P	S	Al	Cr	Ni	Mo	Cu	V	Nb	Ti	N	B	Fe
CR1900T	332	543	644			38	337	432	195						2	Bal.

[a]) batch-specific data provided by manufacturers

Table 2
Mechanical properties for different material zones.

	$R_{p0.2}$, MPa	R_m, MPa	A_g, %	A, %
CR1900T, BM	1395	2042	3.9	4.8
CR1900T, SHAZ	957	1015	4.6	15.5

This leads to theoretical values for the shear test 45° of $\eta = \frac{1}{\sqrt{15}} \approx 0.258$ and $\xi = \frac{6\sqrt{15}}{25} \approx 0.93$.

Because of the Gleeble process, no material of sufficient size for a punch test could be provided.

The specimens were tested at room temperature under quasi-static loading with a testing speed of 0.25 mm/second according to DIN EN ISO 6892–1 to determine the mechanical properties. The testing machine was an Instron 5985 Universal testing machine. The ends of the specimens were clamped with hydraulic wedge grips and in the case of the uniaxial tensile test and notched tensile test rigidly connected to the testing machine. The two shear specimens were connected with a rotational degree of freedom around the axis perpendicular to the flat surface of the specimen. This prevents bending, which can occur at the sharp tips of the notches for these types of shear tests. The specimens were prepared with a speckled pattern to capture the displacements during loading with digital image correlation (DIC), which was conducted with the software GOM ARAMIS.

2.2. Numerical procedures

2.2.1. Finite element model

The finite element analyses in this study were performed using LS-Dyna R12 Explicit solver. Three types of finite element analyses were performed. First, the four specimen geometries were simulated with solid elements. The results of the solid element simulations are presented in Section 3.1. Second, the four specimens were simulated with shell elements. These results are presented in Section 3.2 and Section 3.3. Third, the results of the solid and shell element simulations were compared in Section 3.4. Additionally, a flat tensile test with a spot weld in the center was simulated and its results are presented in Section 3.5. This type of specimen can be produced by spot welding a small square piece of steel sheet to a larger steel sheet and then separating the two sheets by carefully cutting and then grinding off the small square piece. The larger sheet that remains exhibits the softened heat-affected zone, the heat-affected zone and parts of the weld nugget. The final contour of the flat tensile test can be extracted from this larger sheet [25]. In the current study, only a simulation of this experiment was performed, no experimental data were obtained. The simulation compares four different discretizations of the specimen and examines the differences in results from the perspective of mesh sensitivity. The simulation reflects realistic results by matching the global displacement to results in the literature [25].

Fig. 2 illustrates the boundary conditions for the simulations. The boundary conditions are the same for solid simulations, shell simulations and the flat tensile test with a spot weld. All nodes at the lower clamped side of the specimen (NFIX) are fixed in space and have zero degrees of freedom. The nodes on the upper clamped side (NMOV) are fixed in z-direction and move in y-direction (longitudinal-direction) with velocity $v_0 = 0.01 \frac{m}{s}$. For the uniaxial tensile test (ut) and the notched tensile test the x-direction (width-direction) is also fixed, while for both shear tests the nodes NMOV can move in width-direction. None of the simulations use a symmetry condition. For all simulations a full model was used. This allowed to place one element at the exact center of specimen. This center element has a size of 0.1 mm× 0.1 mm× 0.1 mm

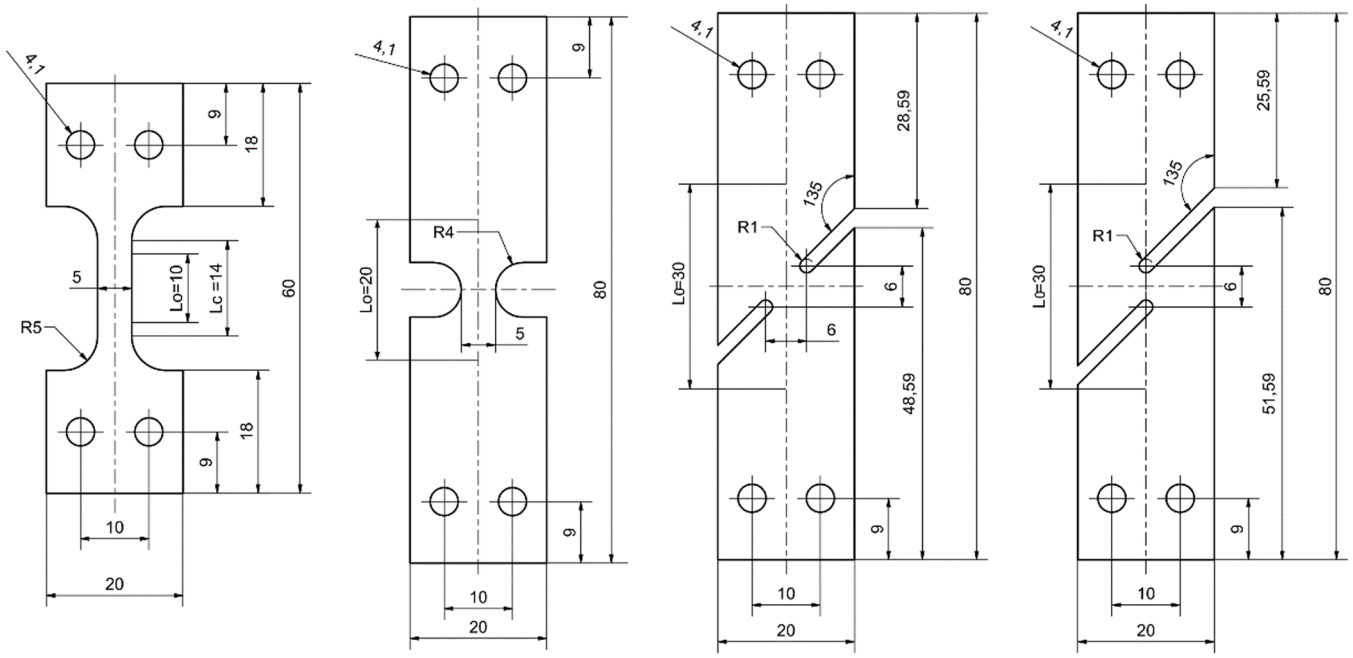


Fig. 1. Specimen geometries for uniaxial tensile test (ut), notched tensile test with 4 mm radius (ntR4), shear test with 45° angle (sh45) and shear test with 0° angle (sh0).

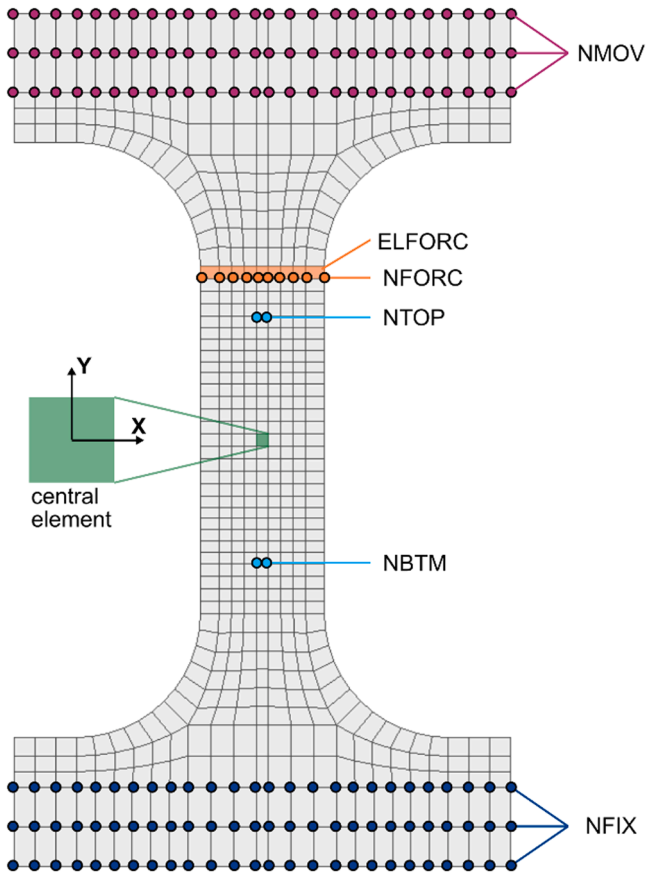


Fig. 2. Boundary conditions of finite element analysis.

for the default solid element simulations, and a size of 0.5 mm× 0.5 mm for the default shell element simulations which were used for the calibration of the material models. The surrounding elements also matched this size as close as possible. This allows for the plastic deformation to distribute symmetrically in the longitudinal-direction and concentrate into one row of elements. The resultant forces are evaluated at the cross section defined by the node set NFORC and its related elements ELFORC. Nodes are placed at the upper (NTOP) and lower (NBTM) positions of the gauge length. These nodes are used to determine the global displacement.

For solid elements, the element formulation ELFORM= 1 was used, which is an element with eight nodes and one integration point positioned at the center of the element. Default hourglass control is used with the keyword *CONTROL_HOURGLASS, adding stiffness to the hexahedral solid elements. For the shell element simulations, ELFORM= 16 was used, which is a fully integrated shell element with four nodes. The Gauss integration points are located at four positions of the shell element face with five through-thickness integration points for a total of 20 integration points. It is proven to be effective to use the option ICRQ= 1 in the keycard *CONTROL_SHELL, which averages plastic strain across element edges and option ISTUPD= 4, which allows for thickness change of the shell elements and neglects elastic strains for the calculation of the updated thickness. For the shell elements, the *CONTROL_HOURGLASS keyword was set to use the stiffness form of type Flanagan-Belytschko (IHQ=4, QH=0.1). These options are specific to LS-Dyna. All solvers offer different options to deal with the shortcomings of 2D simulations.

For the solid model of the shear test 0°, one modification had to be made to the discretization. The mesh discretization was done in a way that the mesh is oriented along the localized band during deformation. For this purpose, the solid elements of the shear specimen 0° were angled 8° in respect to the direct line connecting the center of the two notches. By using an inclined mesh, the plastic strain will concentrate into a narrower band of elements, which allows for the plastic strains to grow faster. This was the only way to achieve a calibration of the fracture locus to match the experimental results. For the shell model of the shear test 0°, the elements were kept aligned with the notch geometry.

The time steps were between 8E-6 and 8E-5 for both the solid and shell element simulations. No mass scaling was used, which led to low values of kinetic energy despite the high velocity. The evolution of energy over time is plotted in Fig. 3. The time axis is normalized using the time of failure.

2.2.2. Material model

The Swift-Voce model is a commonly used constitutive model for isotropic ductile steel sheet metals. The parameters of the Swift model Equation (2) are $\boldsymbol{A}$, $\bar{\varepsilon}_0$ and $\boldsymbol{n}$. The Voce model Equation (3) uses the parameters $\boldsymbol{k_0}$, $\boldsymbol{Q}$ and $\boldsymbol{\beta_0}$. The two models are combined with a factor $\boldsymbol{\alpha}$ for the Swift model and a factor $(\boldsymbol{1}-\boldsymbol{\alpha})$ for the Voce model to form the Swift-Voce model.

$$\bar{\sigma}_y^S = \boldsymbol{A}\cdot\left(\bar{\varepsilon}_0 + \bar{\varepsilon}^{pl}\right)^{\boldsymbol{n}} \tag{2}$$

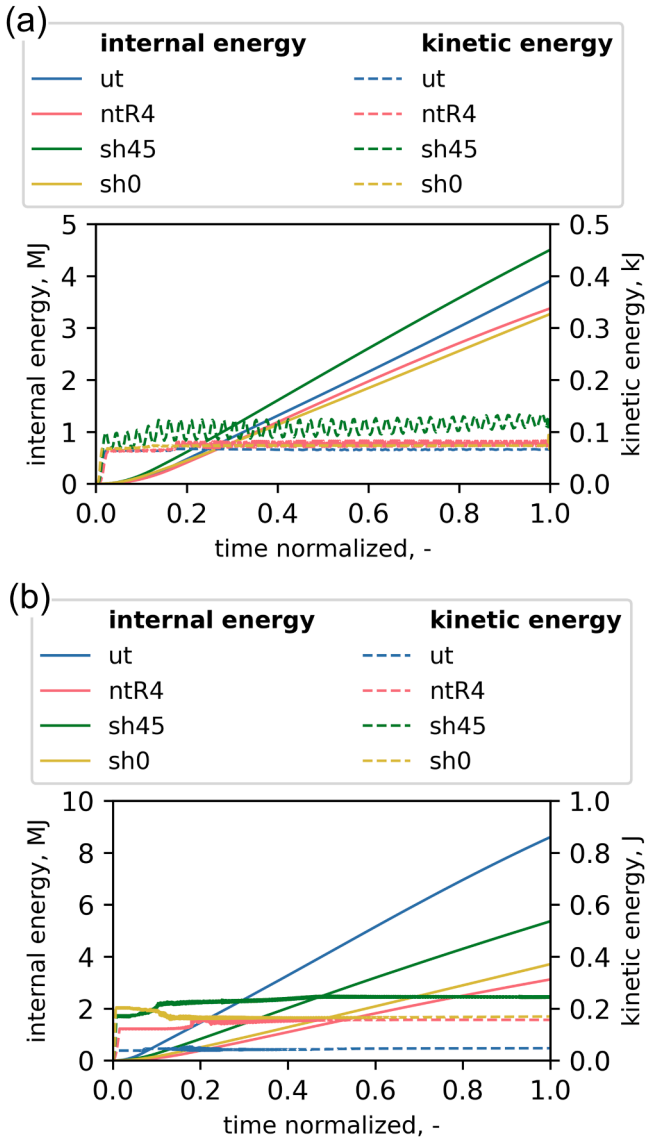


Fig. 3. Evolution of kinetic and internal energy over normalized time for the finite element simulations with a) solid elements and with b) shell elements.

$$\bar{\sigma}_y^V = k_0 + Q\cdot\left(1 - e^{-\beta_0\bar{\varepsilon}^{pl}}\right) \tag{3}$$

$$\bar{\sigma}_y^{S-V} = \alpha\cdot A\cdot\left(\bar{\varepsilon}_0 + \bar{\varepsilon}^{pl}\right)^n + (1-\alpha)\cdot\left[k_0 + Q\cdot\left(1 - e^{-\beta_0\bar{\varepsilon}^{pl}}\right)\right] \tag{4}$$

The material in the softened heat-affected zone exhibits a yield plateau with a constant strength when plastic deformation begins. This was accounted for by replacing the beginning of the Swift-Voce curve with a linear segment.

The parameters of the Swift-Voce model were calibrated with an inverse approach using the uniaxial tensile test (ut) and are listed in Table 3. Separate sets of parameters were calibrated for solid elements and shell elements.

A phenomenological damage model was selected to calculate damage accumulation dependent on the stress state and to predict the strain to fracture. The Hosford Coulomb model was selected because it only uses four parameters a, b, c and n_f [30]. The equation for the Hosford Coulomb model is given in Equation (5). Parameter n_f is commonly set to 0.1, leaving only three parameters that need to be calibrated. All four specimen geometries described in Section 2.1 were simulated in LS-Dyna to inversely determine the three parameters of the fracture locus. The resulting parameters for the softened heat-affected zone are listed in Table 4. Again, separate sets for shell and solid elements are provided. The simulations in this study focus on the modeling of the softened heat-affected zone material and the fracture prediction in this zone. Therefore, the Hosford Coulomb parameters for the base material are not listed in Table 4.

Table 4
Parameters of Hosford Coulomb fracture locus for softened heat-affected zone [29].

Material	a	b	c
CR1900T, SHAZ, Solids	1.95	1.0	0.08
CR1900T, SHAZ, Shells	1.518	0.555	0.034

$$\varepsilon_f(\eta,\ \bar{\theta}) = b\cdot(1+c)^{\frac{1}{n_f}}\cdot\left[\left\{\frac{1}{2}\left((f_1-f_2)^a + (f_2-f_3)^a + (f_3-f_1)^a\right)\right\}^{\frac{1}{a}} + c\cdot(2\eta + f_1 + f_3)\right]^{-\frac{1}{n_f}} \tag{5}$$

With parameters f_1, f_2, f_3:

$$f_1(\bar{\theta}) = \frac{2}{3}\cos\left(\frac{\pi}{6}(1-\bar{\theta})\right), f_2(\bar{\theta}) = \frac{2}{3}\cos\left(\frac{\pi}{6}(3+\bar{\theta})\right), f_3(\bar{\theta}) = -\frac{2}{3}\cos\left(\frac{\pi}{6}(1+\bar{\theta})\right).$$

The stress state is described by triaxiality η, Lode angle parameter $\bar{\theta}$ and equivalent plastic strain ε_{eq}^{pl}. The triaxiality η is defined as the ratio between the volumetric stress p and the von Mises equivalent stress σ_e. The principal stress values are the maximum principal stress σ_1, the intermediate principal stress σ_2 and the minimum principal stress σ_3. The Lode angle parameter $\bar{\theta}$ is calculated from the Lode parameter ξ, which relates the third deviatoric stress invariant J_3 to the von Mises equivalent stress. An additional parameter can also be found in the literature as the Lode parameter L described in Equation (13).

$$p = -\sigma_m = -\frac{1}{3}(\sigma_1 + \sigma_2 + \sigma_3) \tag{6}$$

$$q = \sigma_e = \sqrt{\frac{1}{2}\left[(\sigma_1-\sigma_2)^2 + (\sigma_2-\sigma_3)^2 + (\sigma_3-\sigma_1)^2\right]} \tag{7}$$

$$r = \left[\frac{27}{2}(\sigma_1-\sigma_m)(\sigma_2-\sigma_m)(\sigma_3-\sigma_m)\right]^{\frac{1}{3}} \tag{8}$$

$$\eta = -\frac{p}{q} \tag{9}$$

$$\xi = \left(\frac{r}{\sigma_e}\right)^3 = \frac{27}{2}\frac{J_3}{{\sigma_e}^3} \tag{10}$$

$$\xi = \cos(3\theta) \tag{11}$$

$$\bar{\theta} = 1 - \frac{2}{\pi}\arccos(\xi) \tag{12}$$

$$L = \frac{3\tan(\theta) - \sqrt{3}}{\tan(\theta) + \sqrt{3}} = \frac{2\sigma_2 - \sigma_1 - \sigma_3}{\sigma_1 - \sigma_3} \tag{13}$$

Furthermore, under a plane stress condition, the fracture locus can be simplified from a surface to a 3D curve. Triaxiality η and Lode parameter ξ are uniquely related according to Equation (14) for the plane stress condition.

$$\xi = -\frac{27}{2}\eta\cdot\left(\eta^2 - \frac{1}{3}\right) \tag{14}$$

The Generalized Incremental Stress State dependent damage Model (GISSMO) provides a material model that can be used to transfer damage calculated from forming simulations to crash simulations [31,32]. By treating the constitutive model and damage formulation separately, it is possible to combine a unified formulation of damage with arbitrary material models. An isotropic von Mises plasticity model is implemented with the keyword *MAT_PIECEWISE_LINEAR_PLASTICITY for LS-Dyna, where the stress-strain values are given in tabular form. Damage accumulation is considered using the keyword *MAT_ADD_EROSION.

$$D = \int_0^{\varepsilon_{eq}^{pl}} \frac{\mathrm{d}\varepsilon_{eq}^{pl}}{\varepsilon_f} \tag{15}$$

Table 3
Swift-Voce parameters for different material zones [29].

Material	A	$\bar{\varepsilon}_0$	n	k_0	Q	β_0	α	Yield plateau
CR1900T, BM, Solids	2900	0.001	0.08	1107	1030	122	0.3	
CR1900T, SHAZ, Solids	1915	0.001	0.18	719	361	53	0.11	[0., 0.023] [960., 970.]
CR1900T, BM, Shells	2900	0.001	0.07	1057	1030	130	0.28	
CR1900T, SHAZ, Shells	1225	0.001	0.18	740	395	53	0.11	[0., 0.022] [960., 960.]

For the GISSMO failure model, damage is nonlinearly incrementally accumulated according to Equation (15). The strain to failure ε_f was integrated in this keyword as a function according to Equation (5). For simplification purposes, the coupling of damage to stress was suppressed by setting the option *DMGTYP* = 0 for the GISSMO model in this study. Failure of an element is assumed when the value of D reaches 1. Although no coupling of damage to stress was used, it can be assumed that the presented regularization method can be adapted for damage models with stress coupling, as the regularization criterion is displacement-based. A change in damage model would change the magnitude of the regularization, but not the mesh-size dependence. The predicted values of maximum engineering strain are compared to the experimental mean values (Table 5). The relatively large deviations for ntR4 stand out (−17.1% solids, −11.5% shells). These deviations can likely be attributed to anisotropic behavior caused by the relatively thick AlSi-coating. Moreover, shell models are unable to accurately resolve large thickness strains, such as those occurring in the ntR4 specimen.

2.2.3. Regularization

The crack band approach is a regularization technique for finite element simulations that has been developed in the context of brittle materials such as concrete [7,9,33]. The underlying idea of the crack band approach can be described as follows. When the crack band is formed and the crack is modeled with a single row of elements, then the crack opening displacement will be equivalent to the displacement of that single element.

This idea was motivated by the equation used to calculate the fracture energy G_F (Equation 16). It is calculated by the dissipated energy per unit volume g_F times the volume described by the height of the crack band h_b and the cross-sectional area A. Here G_F is the dissipated energy in Joule, and G_f is the dissipated energy per cross-sectional area in $J{\cdot}mm^{-2}$.

$$G_F = A h_b g_F \tag{16}$$

$$G_f = \int_{\bar{\varepsilon}_0^{pl}}^{\bar{\varepsilon}_f^{pl}} l_c{\cdot}\sigma_y{\cdot}d\bar{\varepsilon}^{pl} = \int_0^{\bar{u}_f^{pl}} \sigma_y{\cdot}d\bar{u}^{pl} \tag{17}$$

This approach has been discussed previously by Hillerborg [20], who concluded that it is preferable to describe a failure criterion dependent on the displacement and not strain (Equation 17). The reasoning behind this is the same as why a fracture strain is always given with a gauge/reference length. If the height of the necking zone is fully enclosed in the reference length, the measured strain depends on the reference length. However, the plastic displacement does not depend on the reference length and remains constant. In [34], the principal strain direction is used to estimate the crack opening direction. Because the mesh is not necessarily oriented congruently with the localized zone, the projected length of the element is used. The projected length of the element in principal direction is then assumed to be the characteristic length of the element and is used to determine the regularization factor. This simplification applies to fracture occurring in K_I-mode, where the crack opens in the direction of the crack band height. In [35] the outer corners of an element are used to measure the projected length. In order to deal with arbitrarily shaped elements, we propose to project the length of two diagonal corners of a quadrilateral element as shown in Fig. 4. As there are two diagonal corner pairs, we can use the average of the two projected lengths (Eq. 18). This improves the approximation of the characteristic length for certain element shapes.

Table 5
Comparison between experimental maximum engineering strain and prediction of finite element simulation.

	ut	ntR4	sh45	sh0
Exp.	0.1696	0.02776	0.05191	0.07450
Sim. (Solids)	0.1500	0.03252	0.04941	0.07005
Sim. (Shells)	0.15991	0.03095	0.05848	0.07469
Deviation (Solids)	11.6%	-17.1%	4.8%	6.0%
Deviation (Shells)	5.7%	-11.5%	-12.7%	-0.3%

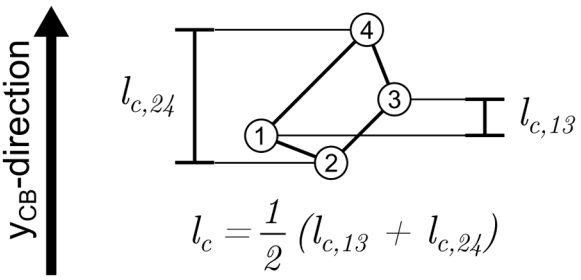


Fig. 4. Calculation of characteristic length by projecting diagonal corner nodes onto crack band direction.

$$l_c = \frac{1}{2}\left(l_{c,13} + l_{c,24}\right) \tag{18}$$

In this study, we discuss the crack band approach in the context of ductile materials and for cases in which failure is driven by shear deformation. When the deformation contains a simple shear component, the principal strain direction is not suitable for determining the crack band orientation. The crack opening direction must be separated into two components, one in the tensile direction and one in the shear direction. For a coaxial deformation, the crack opening direction is assumed to be identical to the principal strain direction. The crack opening direction is updated to follow the principal strain direction during deformation. For a fracture resulting from sliding mode K_{II}, the displacement in Equation (17) needs to be replaced by the shear opening displacement. For ideal simple shear, the shear opening direction is assumed to be shifted 45° from the principal stress direction, where the direction of the shift is toward the direction of principal strain. For other non-coaxial deformations, determining the shear opening direction is not as straightforward and the shifting angle differs from 45° [23,24]. While using the principal strain direction to determine the crack opening direction for coaxial deformations is an established method [8,17], a definitive approach for non-coaxial deformations has not yet been established. The accuracy of decomposing the crack opening direction into a tensile and shear part was neither tested nor verified in the current study.

We introduce a new coordinate system that has its origin in the geometric center of the specimen and its axes are fixed to the localized band. The y_{CB}-axis is along the height of the localized band, the x_{CB}-axis is along the width of the band, and the z_{CB}–axis is oriented along the sheet thickness (Fig. 5). For the considerations in this study, it is

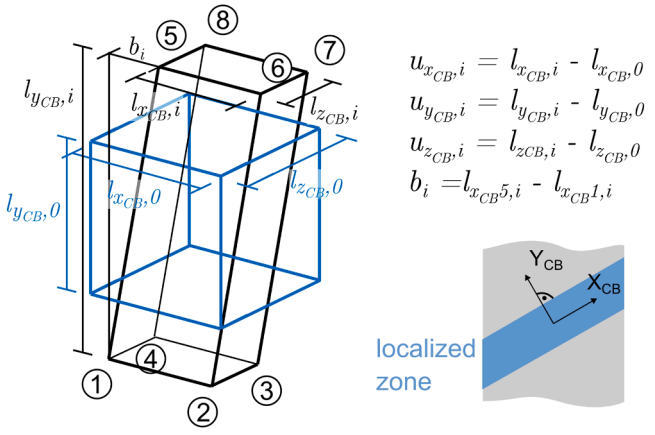


Fig. 5. Displacements at state i in coordinate system fixed and aligned with crack band.

assumed that the direction of simple shear is aligned with the x_{CB}-direction. The displacements separated in coaxial stretch and simple shear directions can then be calculated according to the equations in Fig. 5.

In Section 3.4, the results of the shell element simulations are compared with those of solid element simulations. To this end the field values in a block consisting of a large number of small solid elements are averaged to one single value. To obtain the averaged values for equivalent plastic strain ε_{eq}^{pl}, triaxiality η and Lode parameter ξ the following equation was used.

$$\eta_{avg} = \sum_{i=0}^{n} \frac{v_i \cdot \eta_i}{V_{block}} \tag{19}$$

In Equation (19) variable n is the number of solid elements in the block, v_i is the volume of a single solid element i and η_i is the triaxiality of this element. The sum of the single elements' values is averaged over the volume of the full block V_{block}.

The displacements of the corner nodes of the block are used to calculate the y_{CB}-displacement of the full block. Describing an average value for the shear opening displacement b is not as straightforward, because the block deforms into an S-shape. Therefore, the average value b_{avg} for the block was calculated for each row k of the block b_k according to the equation in Fig. 5. The values were then multiplied by the height of each row h_k and averaged over the full height of the block h_{block}. Variable m is the number of rows k in the block. The equation for calculating b_{avg} is presented in Equation (20).

$$b_{avg} = \sum_{k=0}^{m} \frac{h_k \cdot b_k}{h_{block}} \tag{20}$$

3. Results & discussion

3.1. Aspect ratio of solid elements

In this section, we examine the effect of element aspect ratio on the calculation of damage and

focus on the notched tensile specimen. The specimen was modeled using solid elements. In the center of the specimen, where the formation of the localized band is expected, three variations of the discretization were tested (Fig. 6). The full model without symmetry conditions was used, which allows to place one element at the exact center of the model. One element was placed with its centroid exactly on the origin of the model.

The first variation uses perfect cubes. The edge length is 0.1 mm in each direction. This variation is referred to as "cube". Two more variations were used, which were deliberately chosen to have extreme aspect ratios for the discretization, with one side being five times as long as one other side. One variation uses elements of size 0.1 mm in width-direction, 0.1 mm in longitudinal-direction and 0.5 mm in thickness-direction. This variation will be referred to as "long". Another variation uses elements of size 0.5 mm in width-direction, 0.1 mm in longitudinal-direction and 0.5 mm in thickness-direction. This variation will be referred to as "flat". The important criteria for these meshes is that the element size in longitudinal-direction, which is the expected direction of the localized band height and the direction of crack opening, is 0.1 mm for all three variations.

Such extreme aspect ratios are typically not recommended since damage criteria defined with respect to the plastic strain are known to be sensitive to the characteristic length of the elements. The characteristic length of a solid element is defined as the cubic root of the element volume in the standard literature and in most finite element solvers. For the three variations the characteristic length values are 0.1 mm (cube), 0.171 mm (long) and 0.292 mm (flat). The elements referred to as long are almost twice as large as the reference model with cubic elements, and the elements referred to as flat are almost three times as large as the cubic elements.

Fig. 7 shows a cross-section of the deformed meshes and the distribution of plastic strain when the critical plastic strain is reached in the central element. This cross-section cuts the specimen in half along the y-axis (longitudinal axis). The view is directed at the center of the specimen in the yz-plane. The results show, that the curvature of the localized band can be properly represented with all three variations since the element edge length in longitudinal-direction is 0.1 mm for all three variations. This refinement along the localized band ensures a correct calculation of the curvature. Most deformation occurs for the elements in the center. The notched tensile test is meant to characterize the material for a plane strain deformation. However, the deformation does not achieve an exact plane strain condition, since the strain component in width-direction is close but not equal to zero.

Fig. 8 shows another cross-section of the deformed mesh. This time, the specimen is cut along the x-axis (width-axis) and the view is directed at the xz-plane. From this view, we can see that the specimen is slightly curved along the width-axis. The elements in the center (x = 0) shorten more in thickness-direction than the elements at the notches. At the

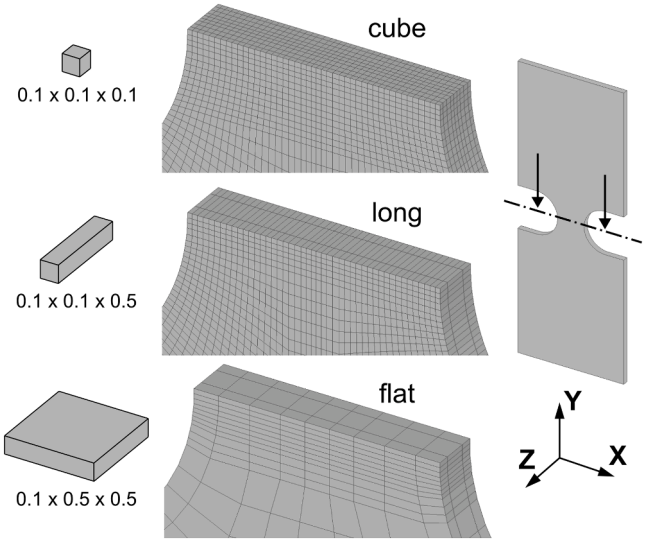


Fig. 6. Finite element models of the notched tensile test meshed with solid elements of varying aspect ratios (cube, long, flat).

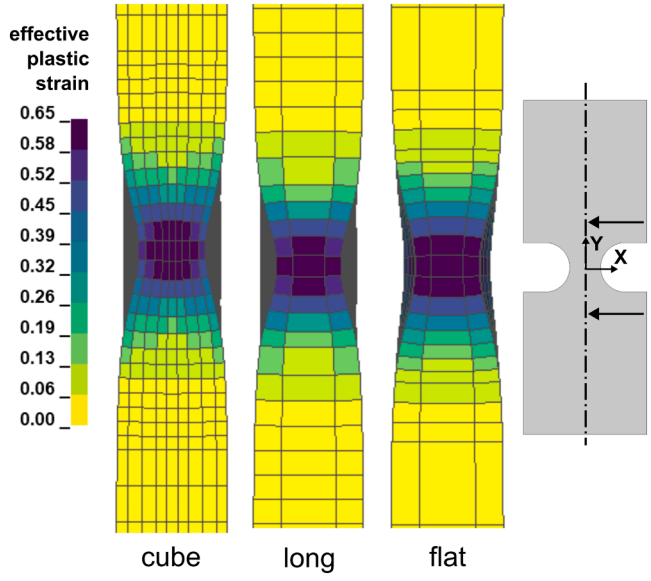


Fig. 7. Side view of necked area in notched tensile test meshed with solid elements of varying aspect ratios (cube, long, flat).

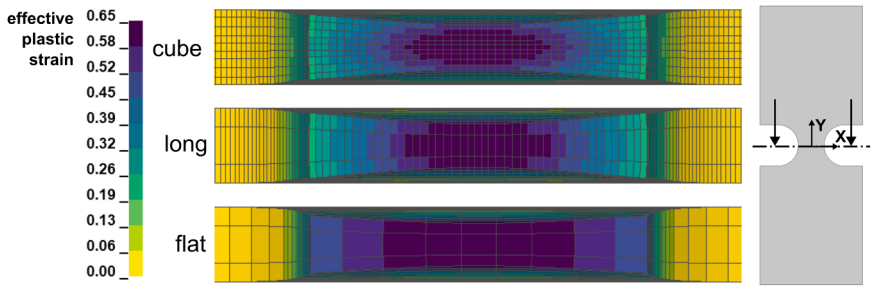


Fig. 8. Top view of necked area in notched tensile test meshed with solid elements of varying aspect ratios (cube, long, flat).

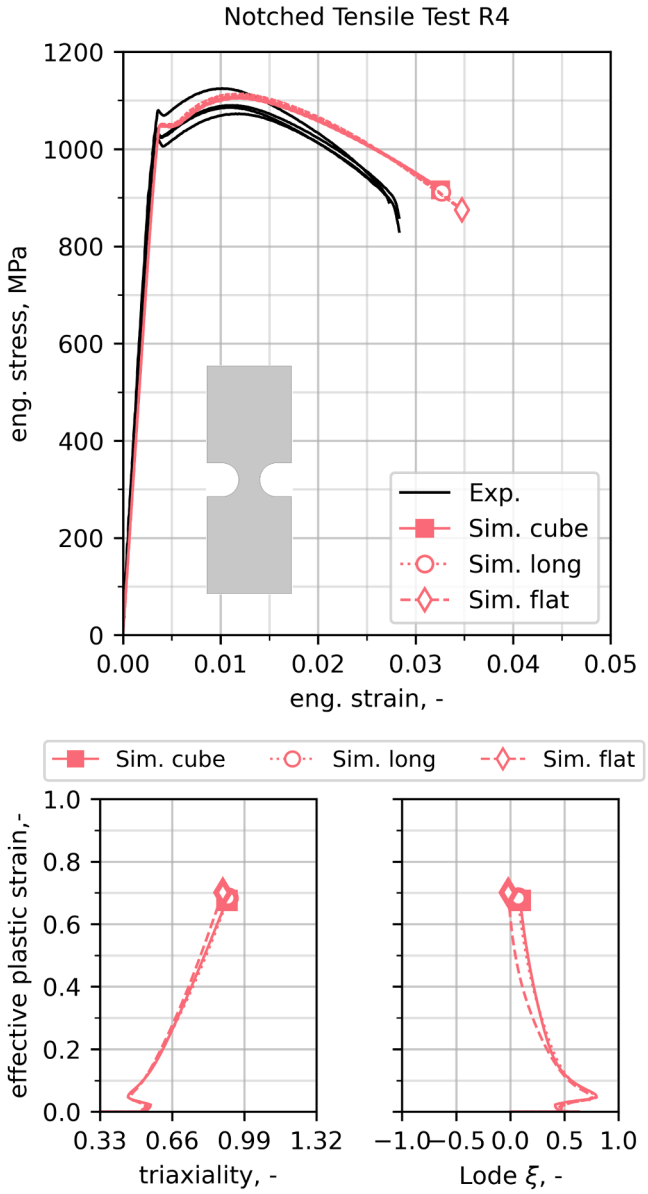


Fig. 9. Global stress strain curve and local strain paths of center element for notched tensile test meshed with solid elements of varying aspect ratios (cube, long, flat).

outer edge of the notched region the elements keep almost a constant length in thickness-direction. For a plane strain deformation, the lengths change only in two directions, that is, the longitudinal- and width-directions in our case. Since we are also assuming an isochoric deformation, the remaining edge length in width-direction would need to remain constant. A closer look reveals that this is not the case.

According to standard literature, the damage criterion must be adjusted for the two variations which exhibit significantly larger characteristic lengths of the critical element. However, the results shown in Fig. 9 reveal that the damage criterion still adequately predicts the failure strain for the two variations "long" and "flat". The predicted softening is almost identical for all three variations. There is some deviation between experimental and simulated softening. This can likely be attributed to an anisotropic effect caused by the thick coating of the steel sheet. The differences in the predicted global failure strains are negligible. They are 0.033 for the cubic element and long element and 0.035 for the flat element which is a deviation of only approximately 6.1%.

For a plane strain condition, the local strain paths are proportional with a triaxiality, Lode parameter pair of (0.578, 0). Triaxiality values above 2/3 indicate a high hydrostatic stress. The resulting strain paths of the three variations show, that at the beginning the Lode parameter is 0.5 and approaches zero at the end of the deformation. The underlying cause has been discussed previously. For a plane strain deformation with a Lode parameter of zero one edge length has to remain constant throughout the deformation, but the specimen slightly contracts in width-direction with the highest contraction in the central element.

The results show that the aspect ratio is not as relevant as standard literature suggests. The determining property is the element edge length in direction of the localized band. The challenges for using shell elements are evident from the results. For shell elements we would typically use elements that are larger than the height of the localized band. The curvature of the localized band will therefore not be reflected in the calculated result. This fact must be considered by empirical correction of the calculated plastic strain.

Fig. 10 illustrates another aspect of the material behavior in the necked region. At failure, the displacement is concentrated into the localized area. Elements outside of the localized band do not contribute to the global displacement. The central layer of elements which had an original section length of 0.1 mm has a displacement of about 0.08 mm, when the maximum global strain of the experiment is reached. When considering three layers at the center with an original section length of 0.3 mm, the displacement is approximately 0.23 mm.

A section with an original section length of 2 mm has a displacement of 0.58 mm. At an original section length of 2 mm the slope of the curve shown in Fig. 10 flattens and a plateau forms. We take a slope of 5% as a criterion to determine the crack band height. A slope of 5% is reached for 2.09 mm. For convenience we take 2 mm to be the crack band height. If we consider larger sections the opening displacement does not increase significantly. This aspect of the material behavior is at the core of the crack band approach. Therefore, shell elements larger than the crack band height are used for regularization. The displacement can then have a constant value irrespective of the element edge length.

The results in this section revealed, that it is not strictly necessary to use elements with equal edge lengths to achieve a good mesh quality. The requirement for the mesh is rather that gradients are sufficiently

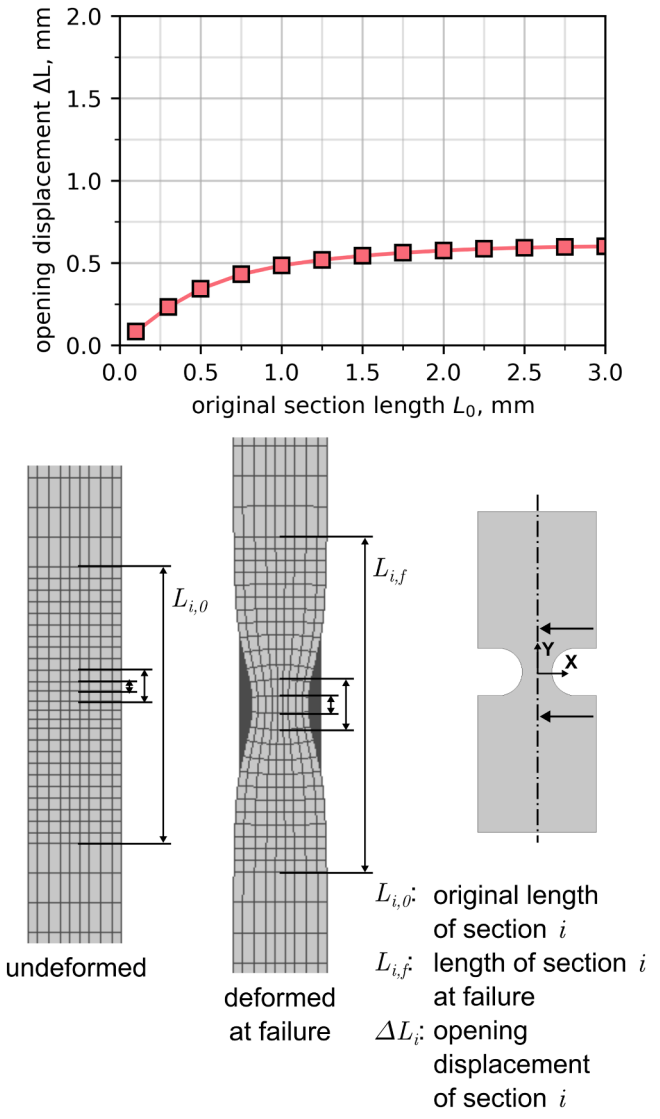


Fig. 10. Displacements along the height in crack opening direction at the center of the notched tensile test meshed with solid cubic elements.

discretized. Therefore, any curvatures must have an appropriate mesh resolution. As a consequence, the aspect ratio has minor influence on the mesh sensitivity if curvatures are sufficiently discretized, and the characteristic length depends on the edge length of the element in the crack opening direction.

3.2. Aspect ratio of shell elements

In this section, the influence of aspect ratio and triaxiality on the 2D finite element analysis with shell elements is discussed. Each specimen was simulated by using three mesh variations. These variations vary in the size of the elements in the localized zone. One variation has square elements with an edge length of 0.5 mm. This is a rather small size when it comes to applications, which use shell meshes. Shell meshes are most commonly used in calculations which need to be optimized toward calculation time. The other two variations have rectangular elements with an aspect ratio of 1.5. One edge is of length 0.5 mm, like the square elements, the other edge has a length of 0.75 mm. The two variations differ in that they are oriented differently. When the longer side is oriented in longitudinal-direction, that is along the height of the localized band, the variation is referred to as "tall". When the longer side is oriented in width-direction, the variation is referred to as "wide".

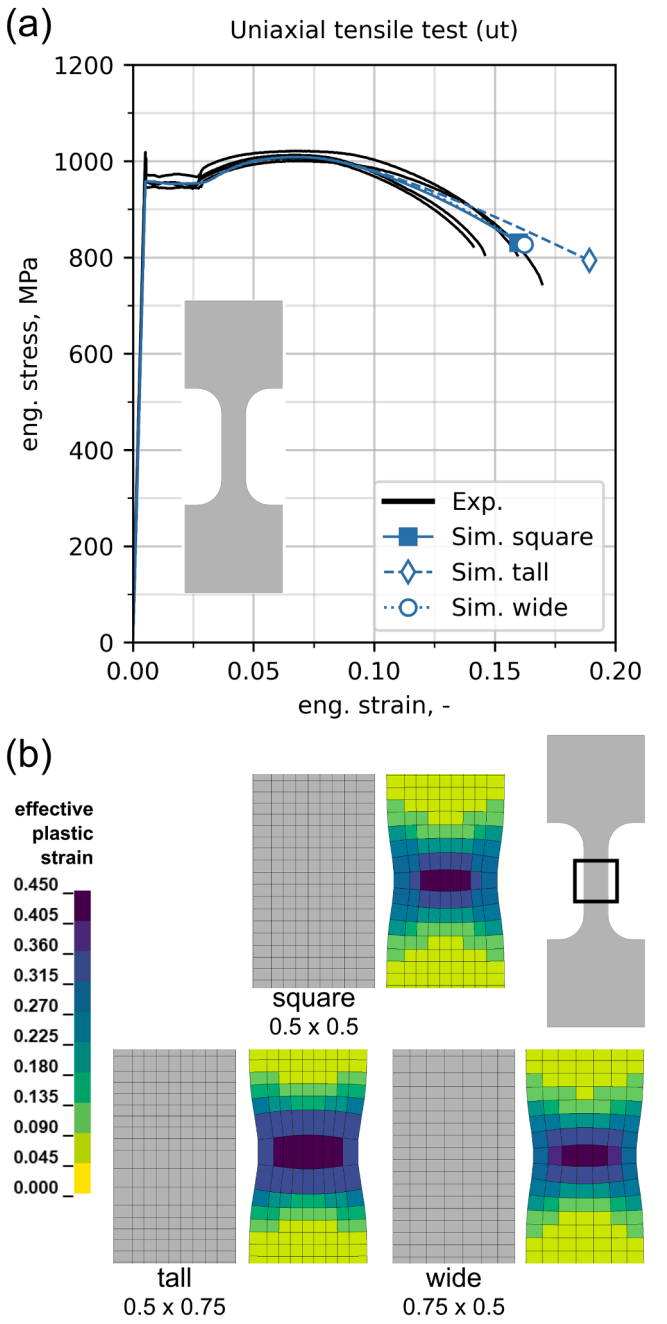


Fig. 11. (a) Experimental and numerical results of uniaxial tensile test. (b) Effective plastic strain distribution at the center of the specimen at failure. Numerical results were obtained with shell elements with three different aspect ratios (square, tall, wide) in the central region.

According to the common description of the characteristic element length, which is calculated by the square root of area, the center element of each variation has the following characteristic length: 0.5 mm for "square" variation and approximately 0.612 mm for the other two variations. The rectangular elements have a 22.5% larger element size than the square elements.

Fig. 11a shows the resulting global stress-strain curve and the distribution of plastic strain at failure for the uniaxial tensile test. The square variation and the wide variation show almost identical results. The difference in softening behavior as well as the difference in global strain are negligible. In contrast the tall variation shows less softening behavior and failure is reached at a larger global strain. The distribution of plastic strain at the time of failure is similar for all three variations

(Fig. 11b). The plastic strain is concentrated into one row of elements for each variation with a value greater than 0.45. The neighboring two rows of elements also exhibit high values of plastic strain with a value of over 0.27.

A discretization of 0.5 mm in longitudinal-direction, i.e. the crack band height, seems to be sufficient to resolve the curvature of the localized band. Since the tall elements have a height of 0.75 mm instead of 0.5 mm the curvature along the height of the band is not sufficiently represented in this variation. The results of the solid element simulations in Section 3.1 showed that the curvature in this area is pronounced. Since this curvature is not adequately represented with shell elements, this leads to a different softening behavior.

The results of the notched tensile test are shown in Fig. 12 and are analogous to the results of the uniaxial tensile test. The softening behavior is the same for variations "square" and "wide" but underestimated for the variation "tall". For the global strain at failure, the "square" and "wide" variations give the same value. The local failure

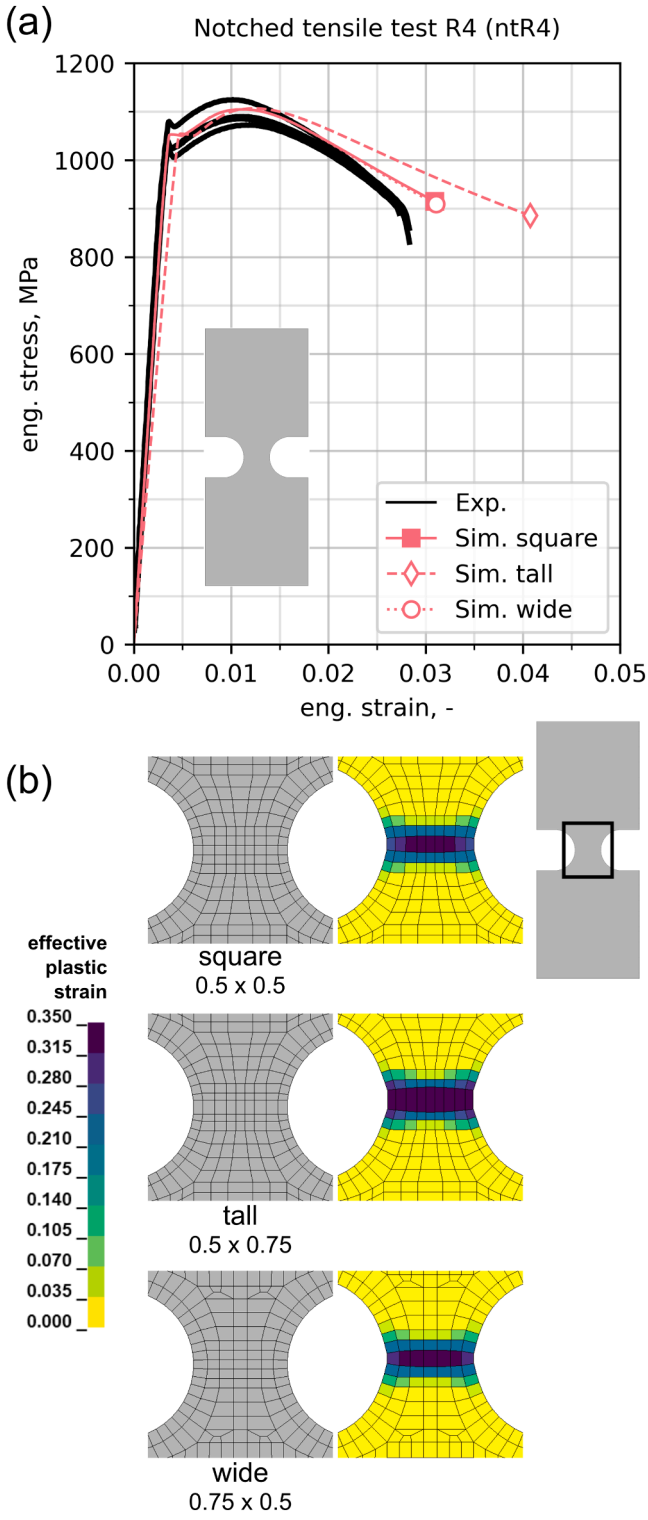


Fig. 12. (a) Experimental and numerical results of the notched tensile test. (b) Effective plastic strain distribution at the center of the specimen at failure. Numerical results were obtained with shell elements with three different aspect ratios (square, tall, wide) in the central region.

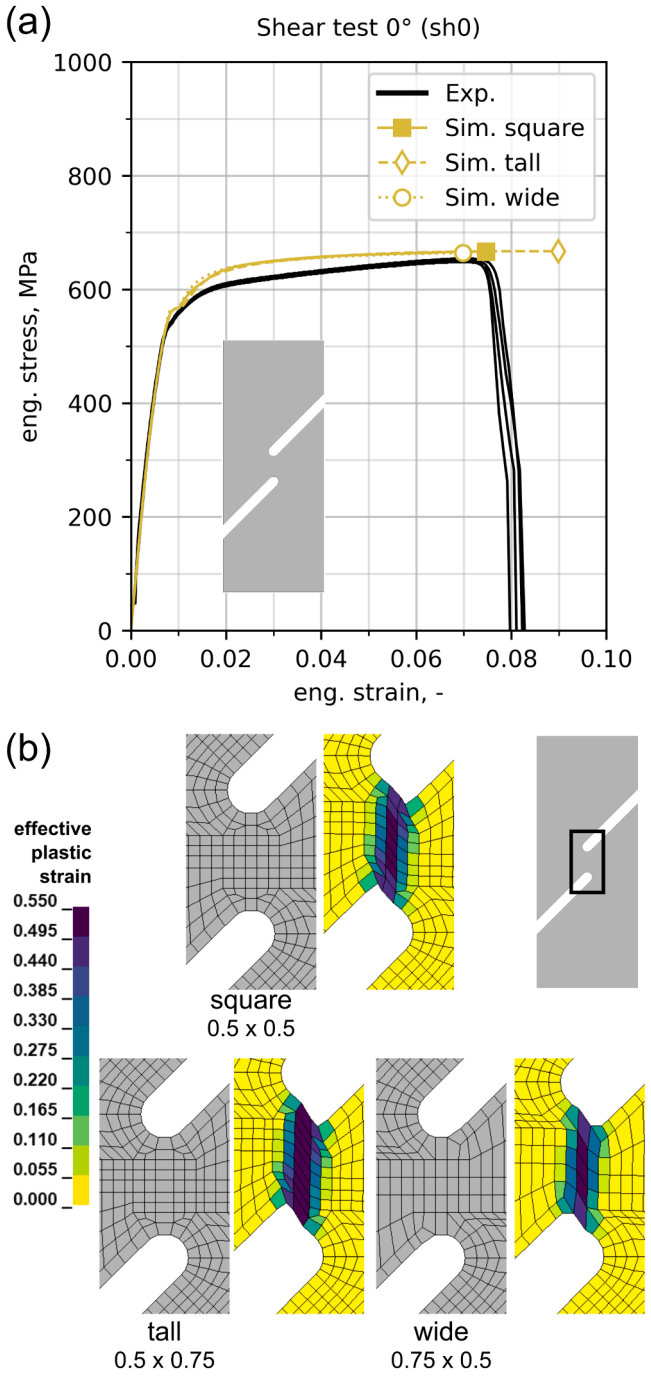


Fig. 13. (a) Experimental and numerical results of shear test with a 0° notch. (b) Effective plastic strain distribution at the center of the specimen at failure. Numerical results were obtained with shell elements with three different aspect ratios (square, tall, wide) in the central region.

strain of the "tall" variation is reached at a higher global strain. It is noticeable that the elastic behavior is also different for the "tall" variation. This might be caused by the geometry of the specimen, namely the notches that cause additional deformational effects that cannot be captured with the "tall" elements.

The results for the shear sh0 specimen are significantly different from those of the uniaxial and notched tensile tests and are shown in Fig. 13. In Section 3.1, it was established that the difference in softening behavior stems from the inadequate representation of the curvature of the localized zone. For this shear test 0°, there is no curvature of the localized band, because the sheet thickness does not change. Consequently, there is no difference between the three variations in the softening behavior. If the simple shear deformation occurred with a perfectly proportional loading path, there would be no change in thickness of the specimen. Moreover, the two edges in shear direction remain parallel and the height of the shear band remains constant. The two parallel edges slide in opposite directions, which is the only source of strain. However, the global failure strain differs for the tall variation. This result implies that the regularization in softening and regularization in failure strain need to be treated separately.

Fig. 14 shows the results for the shear test 45°. The position of the two notches at an angle of 45° angle for the sh45 specimen produce a combination of coaxial stretch and simple shear loading. The softening is overestimated by the shell modeling in comparison to the experimental results. The results are similar to the uniaxial and notched tensile tests. The "square" and "wide" results are almost identical, while the "tall" variation differs in softening behavior and total global strain.

For all specimens, the "square" and "wide" variations showed no difference in softening behavior, although these variations differ significantly in the aspect ratio of mesh in the localized zone and in the characteristic length calculated by the square root of the element area. When the element edge length in crack opening direction was taller, the softening behavior differed for all specimens except for the shear test 0°. In conclusion, the softening behavior is driven by a reduction in the thickness of the localized band. Since there is no thickness reduction when the loading is simple shear, the discretization in crack band opening direction is less important for this specimen. The global fracture strain was always in agreement for the "square" and "wide" variations and always differed for the "tall" variations for all four specimens. The fracture strain is driven by the crack opening displacement, which is along the height of the crack band for tensile opening and along the shear direction for a sliding motion of the crack band. For the shear test 45°, the crack opening direction must be separated into two components, since the deformation is a superposition of simple shear and coaxial stretch.

The specimens were designed to characterize proportional strain paths. In Fig. 15 the actual strain paths obtained, are plotted. The strain paths for the uniaxial tensile test (ut) and the strain paths for the notched tensile test (ntR4) show the greatest variation in triaxiality during loading. The shear test 45° (sh45) strain path runs almost proportional beyond an effective plastic strain of 0.2. The values for triaxiality closely match the theoretical values described in Section 2.1. In the simulation triaxiality is $\eta = 0.258$ and Lode is $\xi = 0.93$, which match the theoretical values up to the second decimal number. A proportional strain path during a superposition of uniaxial stretch (in the plane of non-zero stresses) and simple shear indicates that stretch/shear ratio of elongation is constant. This is the ratio between the stretch perpendicular to the shear direction and the shear opening. The strain paths do not vary significantly with varying aspect ratio of the central element. The last point on each strain path is the point of failure, where the accumulated damage reaches a value of 1.

3.3. Optimized mesh for calibration

The results of the previous sections help to inform the optimization of the mesh discretization. Since for shell simulations the results are solver-

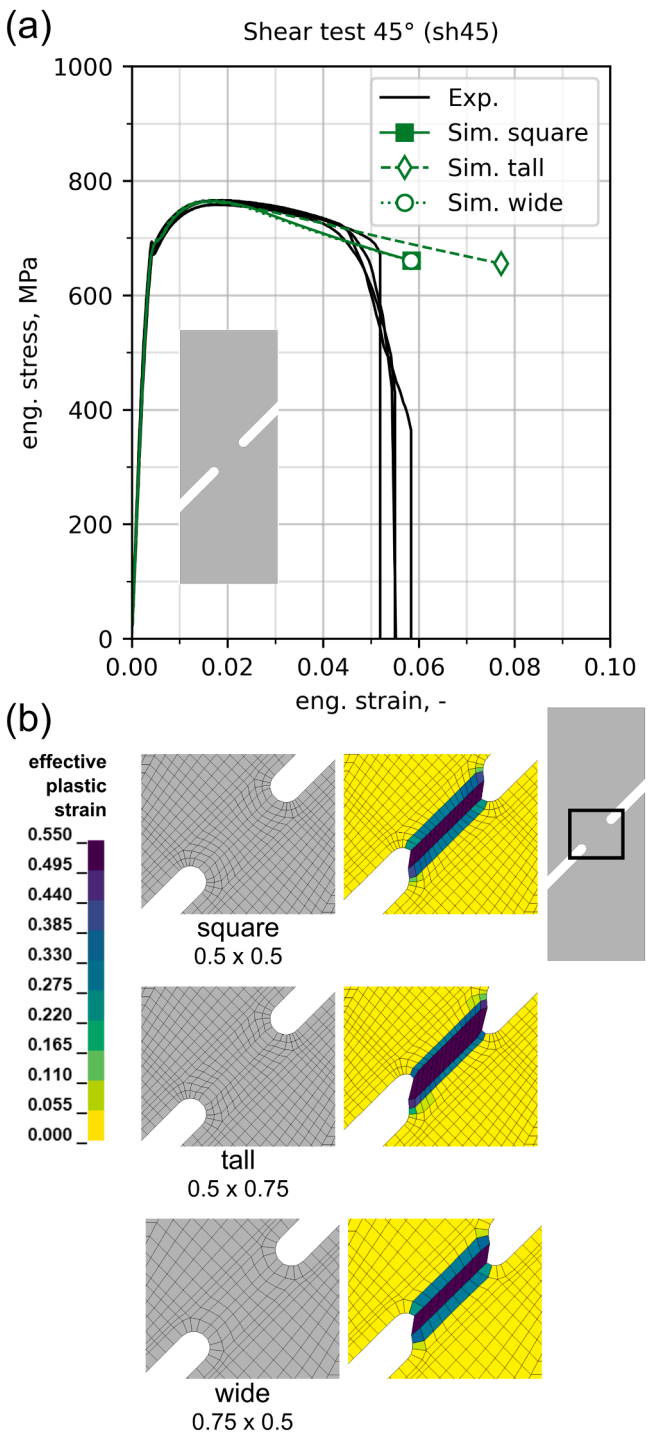


Fig. 14. (a) Experimental and numerical results of shear test with a 45° notch. (b) Effective plastic strain distribution at the center of the specimen at failure. Numerical results were obtained with shell elements with three different aspect ratios (square, tall, wide) in the central region.

specific, the results might not be generalizable to other shell formulations. But for the current study with the described shell settings (see Section 2.2.1) the findings are as follows. It was established that displacement is a better reference value for regularization than strain and that the regularization will be the same for any element size as long as it is larger than the crack band height, which is approximately 2 mm for the material in this study (Section 3.1). It was also established that elements do not need to be square and the aspect ratio is not important as long as the reference length is in crack band height direction (Section

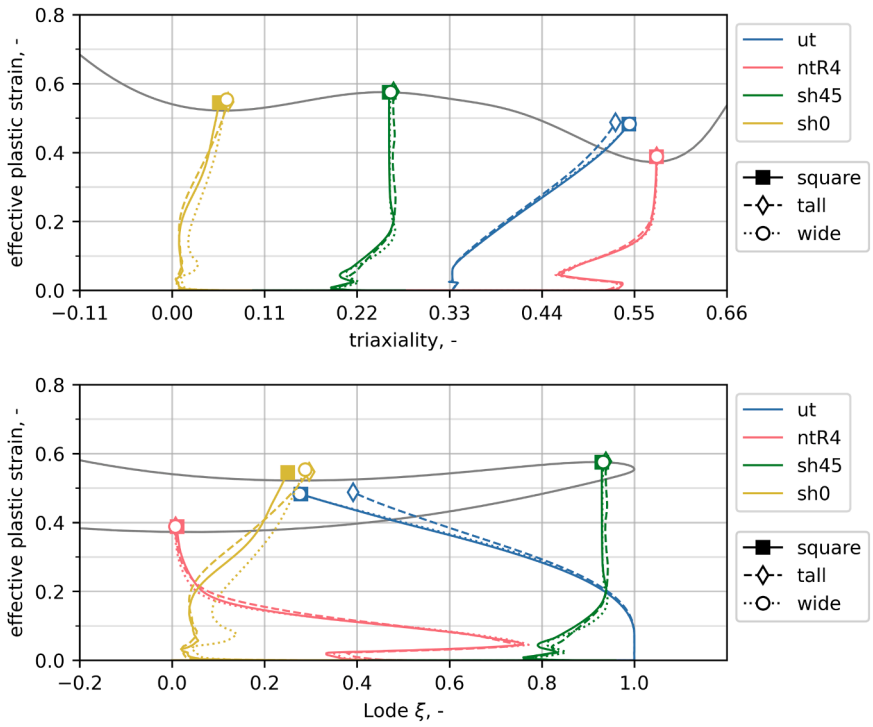


Fig. 15. Strain paths of the central element for four different specimens. Each specimen was discretized with shell elements with three different aspect ratios (square, tall, wide) in the central region.

3.2). It was also observed that softening is likely influenced by necking which is small for sh0 and highest for ntR4 (Section 3.2). The following section suggests how to use these results to optimize the mesh of the calibration test and discusses how the effective plastic strain at the center of the specimen evolves compared to 0.5 mm× 0.5 mm square elements.

The specimens have small geometric dimensions compared to the dimensions of the targeted application in automobile crash analysis. For this present study, it was unfeasible to use larger specimens, since the specimens were cut out from a strip that underwent Gleeble heat treatment. This procedure restricts the possible size of the specimens. Additional geometric demands need to be met to achieve proportional strain paths at specific strain rates. These demands lead to the small dimensions at hand. The width at the specimen center is only 5 mm for the uniaxial and the notched tensile tests and only 4 mm for the shear specimen sh0. Therefore, it is suggested to use elements of 2 mm length in crack band height and of 0.5 mm across the width of the specimen. The rather large aspect ratio of 4 is not expected to have any negative effects due to the previously discussed results.

The edges of the notches for the shear specimens are only 2 mm apart and the notch radius is 1 mm. Therefore, it is not possible to adequately discretize these specimens with 2 mm square elements to perform the calibration. A transition between the large center elements and smaller elements closer to the notches was created. In this way small elements are positioned along the radius at the notch which have almost square dimensions of 0.5 mm× 0.5 mm.

During deformation, small geometric shapes can form that were not present at the start of the deformation. An example is the necking which is a curvature in the thickness direction of the specimen. However, this effect can also occur along the edges of the specimen where the plastic strain of the localized zone meets the edge of the specimen. The mesh should be resolved in such a way that up to uniform elongation the stress-strain curve is closely followed to minimize this sort of effect. The goal is not to mix geometric effects into the regularization and that only softening and fracture strain are considered for regularization.

Fig. 16 shows the results of the uniaxial tensile test with large shell elements of size 0.5 mm× 2 mm in comparison to the results of a simulation with small square elements of 0.5 mm. The outer edge of the specimen deforms (Fig. 16b). As a result, the edge has a dent that cannot be reproduced with a discretization of 2 mm. Therefore, only the elements in the center have a size of 0.5 mm× 2 mm and the element size is decreased towards the edge.

The simulation for the large shell elements is not regularized and the end point has no physical meaning and shows the last point of the simulation. For the large tall shell elements, the softening is not sufficient to capture the experimental behavior. The effective plastic strain distribution is shown at the value of maximum global strain of the experimental results. The highest values are concentrated at the center of the specimen and get small closer to the edges of the specimen. The simulation with small square elements reaches significantly higher values than the simulation with large tall shell elements.

Fig. 17 shows the results for the notched tensile test ntR4. For the discretization of the specimen with large tall shell elements an element size transition towards the edge of the specimen was modeled. When modeled with large elements along the entire width of the specimen, the resulting stress strain curve diverged from the simulation with small square elements for values close to the yield stress. When introducing the transition, the two shell models have almost matching stress-strain curves up until uniform elongation. Compared to the uniaxial tensile test the effective plastic strain distribution shows high values even at the edge of the specimen. Overall, the effective strain is more concentrated than for the uniaxial tensile test.

An element size transition towards the edge was also modeled for the shear test 45° (Fig. 18) and the shear test 0°. The radius at the notch for these two specimens is only 1 mm, therefore a discretization with 2 mm tall elements would result in no curvature at the notch and distort the deformation behavior of the specimens. The softening behavior of the shear test 45° differs significantly from the small shell element simulation. For the shear test 0° the stress-strain curve closely follows the small square element simulation (Fig. 19). All of the simulations with large tall

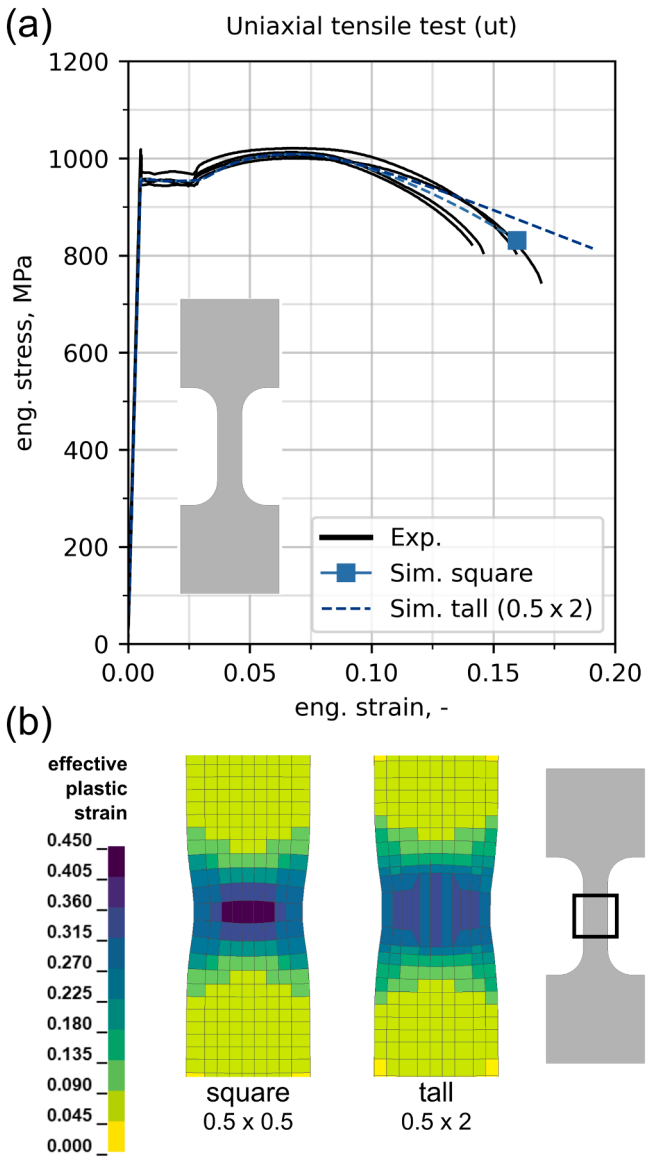


Fig. 16. Experimental and numerical results of uniaxial tensile test. Numerical results have been obtained with modified mesh for calibration of large shell elements a) resulting stress-strain curve and b) distribution of effective plastic strain at maximum engineering strain.

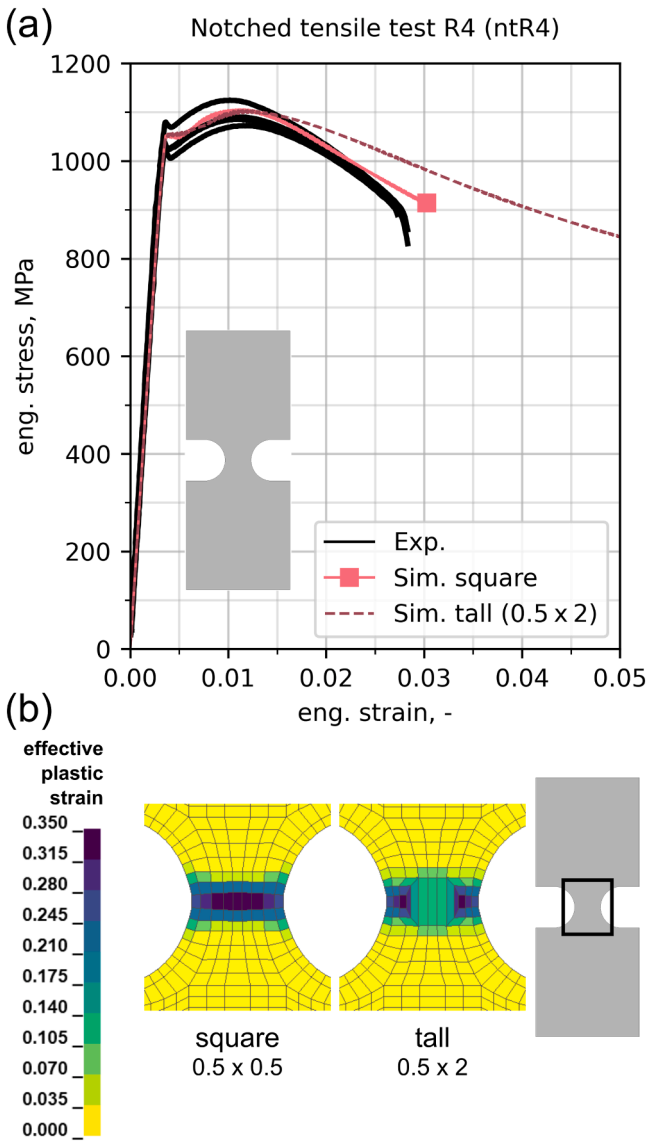


Fig. 17. Experimental and numerical results of notched tensile test R4. Numerical results have been obtained with modified mesh for calibration of large shell elements a) resulting stress-strain curve and b) distribution of effective plastic strain at maximum engineering strain.

shell elements exhibit much smaller effective plastic strain values at the center of the specimen compared to the small square element simulations.

3.4. Small solid vs. large shell elements

In this section, the averaged values over a block of solid elements are compared to the values of a single shell element of the same dimension. For this purpose, the results of the finite analysis with small cube elements of approximately 0.1 mm edge length were used. A block of height 2.0 mm and 0.5 mm width at the center of each specimen was extracted. In the third dimension, the block is equal to the thickness of the steel sheet. This block of elements represents a single tall shell element from Section 3.3 with the same dimensions and at the same location. Ideally, the averaged values from the block of solids would be equal to the values obtained with the single shell element. The averaged values for the block of solid elements were calculated as described in Section 2.2. The shell values were directly output from LS-Dyna.

First the finite element results obtained with the small solid elements for each specimen are shown. The plots show the effective plastic strain, Lode parameter ξ and triaxiality η for every single element in the extracted block. The results for the uniaxial tensile test are shown in Fig. 20, for the notched tensile test R4 the results are shown in Fig. 21. The results of the shear specimens are shown in Fig. 22 (sh0) and Fig. 23 (sh45).

An obvious characteristic of the blocks in both shear specimens is that they bent into an S-shape. The front view for the sh45 specimen shows that the width of the block along the S-shape remains relatively constant, whereas the width of the sh0 specimen is thinner in the middle of the block. The bent shape is a result of the superposed deformation of simple shear and coaxial stretch of the sh45 specimen. It is not possible for a single shell element with four nodes to represent this behavior. A shell element with identical dimensions is deformed into a parallelogram. The edges of the element remain parallel but the inner angles are no longer 90°. The Lode parameter and triaxiality do not indicate any information regarding the simple shear component. The same stress state as that indicated in the shell element can equally be achieved by a

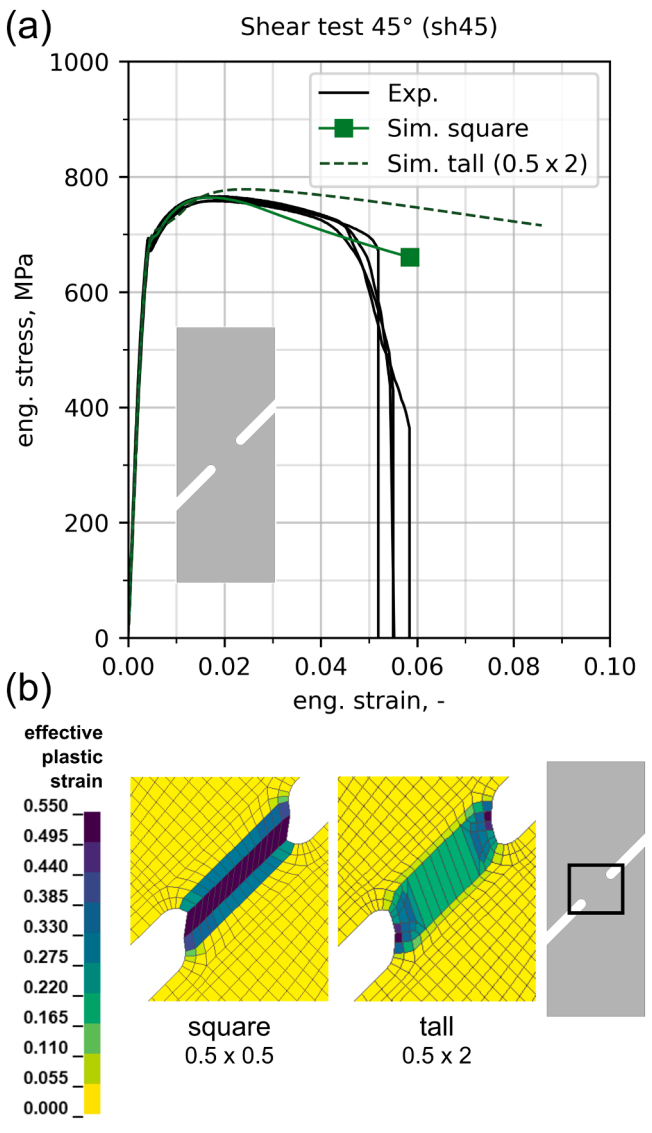


Fig. 18. Experimental and numerical results of shear specimen 45°. Numerical results have been obtained with modified mesh for calibration of large shell elements a) resulting stress-strain curve and b) distribution of effective plastic strain at maximum engineering strain.

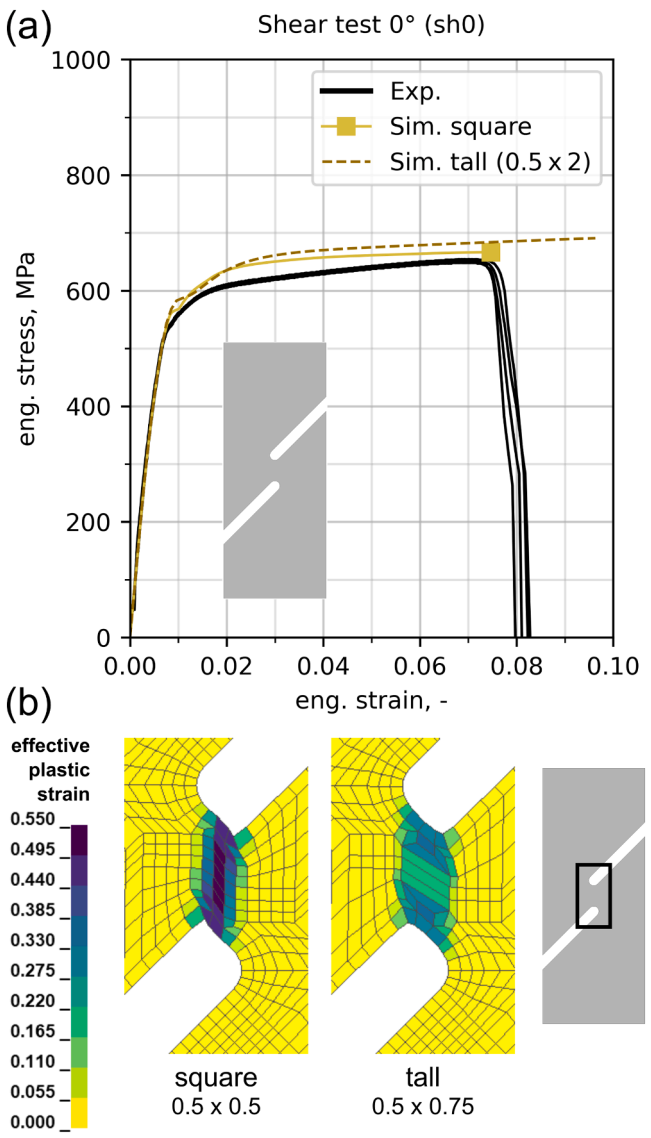


Fig. 19. Experimental and numerical results of shear specimen 0°. Numerical results have been obtained with modified mesh for calibration of large shell elements a) resulting stress-strain curve and b) distribution of effective plastic strain at maximum engineering strain.

coaxial deformation. However, an exclusively coaxial deformation would not result in an S-shaped deformation of the central region. Whether the averaged behavior of a block deformed by coaxial deformation would be close or identical to the averaged behavior of the block deformed by superposed deformation of simple shear and coaxial stretch remains unclear and cannot be answered with the results of this study.

All the plots show that the change of effective plastic strain in x_{CB}-direction (crack band width-direction) is negligible but there is a gradient along the height of the block. This demonstrates that the width of the block and, therefore, the width of the shell element is of minor importance. The plots also show that the effective plastic strain is concentrated in the center and rapidly decreases closer to the upper and lower edges of the block. Except for the uniaxial tensile test, the distribution of effective plastic strain shows values close to zero at the upper and lower edge. All plastic deformation is concentrated within the crack band, which has a height of approximately 2 mm. The side view of the block elements shows that the notched tensile test R4 specimen exhibits the most necking, followed by the uniaxial tensile test. The top views of the shear specimens are distorted because of the bent shape and are not suitable for evaluating the amount of necking that occurs. Therefore, the displacement in thickness-direction of a single layer of elements at the center was extracted at the time of predicted failure. For sh0 the value was - 0.15 mm, for the sh45 it was - 0.24 mm. The sh0 specimen therefore exhibits the least necking. The values of Lode parameter and triaxiality also show that these values are distinct in the center and gradually change along the length of the block. These single element values in each block were averaged for plotting the strain paths. The shell elements predict a single value.

The strain paths of the shell elements and the solid elements of a block section are shown in Fig. 24. The shell and solid models use different Swift-Voce and Hosford-Coulomb parameters, therefore, the following strain path comparisons in Fig. 24 and Fig. 25 should be interpreted qualitatively. Since the shell simulation was not regularized the discrepancy is significant but the comparison indicates the requirements that need to be fulfilled by the regularization. The last point of the strain paths for the block indicates the first element failure. To give some orientation, the point, where the maximum engineering strain of the experimental data is reached, is indicated by a circle for the shell strain paths. The solid block strain paths are the target values for the

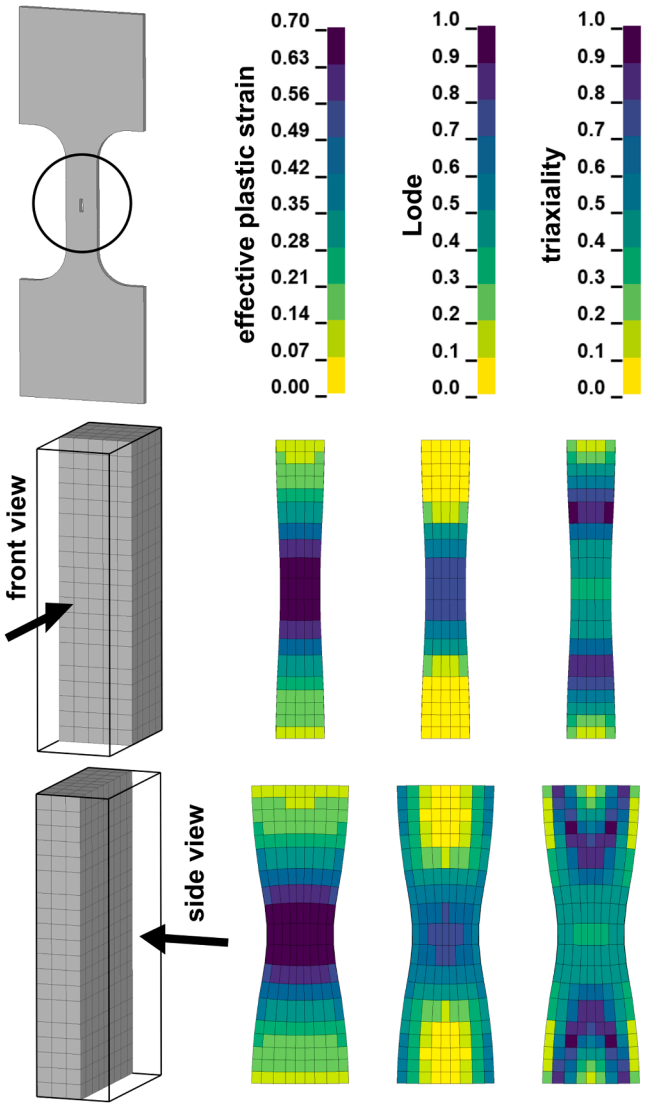


Fig. 20. Distribution of effective plastic strain, Lode value and triaxiality over block of small solids for uniaxial tensile test.

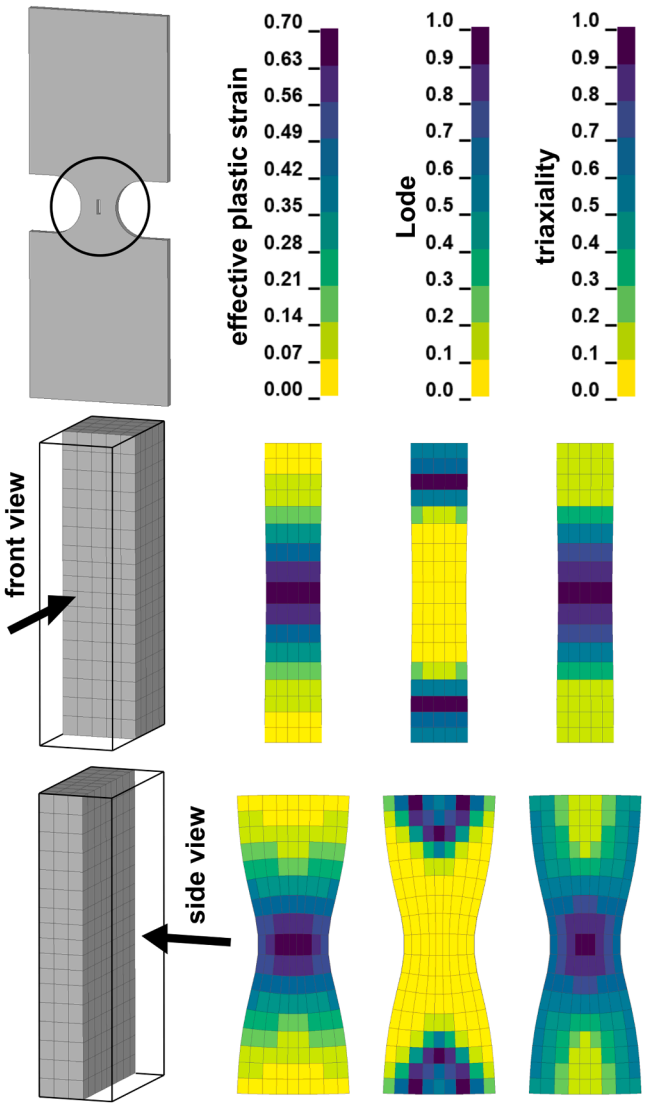


Fig. 21. Distribution of effective plastic strain, Lode value and triaxiality for notched tensile test R4.

regularized shell elements. The closest match between solid block and shell element are the sh45 strain paths. The strain paths are almost proportional. For a superposed deformation of simple shear and coaxial stretch a proportional strain path can be achieved when the coaxial deformation is uniaxial in-plane, i.e. there is only stretch in y_{CB} direction but no change in length in x_{CB}-direction. Additionally, the ratio between the stretch in

y_{CB}-direction and the shear opening b in x_{CB}-direction needs to remain constant during deformation. The effective plastic strain does not increase as fast for the solids as it does for the shells. For the sh0 specimen the strain path of the shell element is almost a perfect simple shear strain path. For the solid block the triaxiality is higher, indicating a superposition with coaxial stretch.

The strain paths for ut and ntR4 show the most significant mismatch between solid block and shell element. For the ut specimen, the strain path for the solid block has a relatively constant value of triaxiality around 0.33, whereas for the shell element the value drifts towards higher values of triaxiality. For the ntR4 specimen the triaxiality for the solid block is also lower than for the shell element, which reaches a value close to 0.577 toward the end, which, combined with the Lode parameter of 0, indicates a plane strain stress state.

For the uniaxial tensile test and notched tensile test, the crack opening direction is along the height of the localized band, i.e. in y_{CB}. direction. For the sh0 specimen the crack opening is in direction parallel to the localized band, i.e. in x_{CB}-direction. For the shear specimen 45°, the crack opening direction has two components. One component in direction of the crack band height (y_{CB}-direction) and the second along the shear direction (x_{CB}-direction). According to the crack band approach the crack opening displacement is preferred to the effective plastic strain as a reference value for regularization. The crack opening displacements versus stress state parameters are plotted in Fig. 25. The effective plastic strain at failure for ut is 0.35 and about 20% higher than for sh45, which has an effective plastic strain at failure of 0.29. The y_{CB}-displacement at failure is almost four times as high for ut (0.88 mm) as for sh45 (0.23 mm). The y_{CB}-displacment for the sh0 shell element is slightly negative, whereas it is positive for the solid block. The shear opening b for sh0 and sh45 are significantly higher than the y_{CB}-displacement values at failure. At failure the shear opening b is higher for sh0 than for sh45. The values of shear opening b at failure for the block 1.32 mm for sh0 and 1.04 mm for sh45 and at the maximum engineering strain for the shell element the shear opening b is 1.26 mm for sh0 and for sh45 it is 1.04 mm. The values for the solid block and the

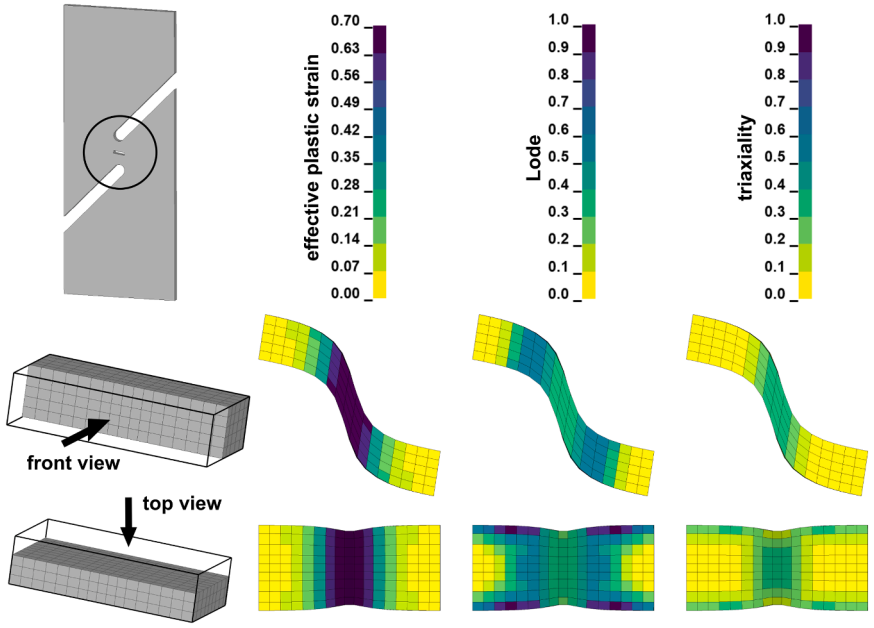


Fig. 22. Distribution of effective plastic strain, Lode value and triaxiality for shear test 0°.

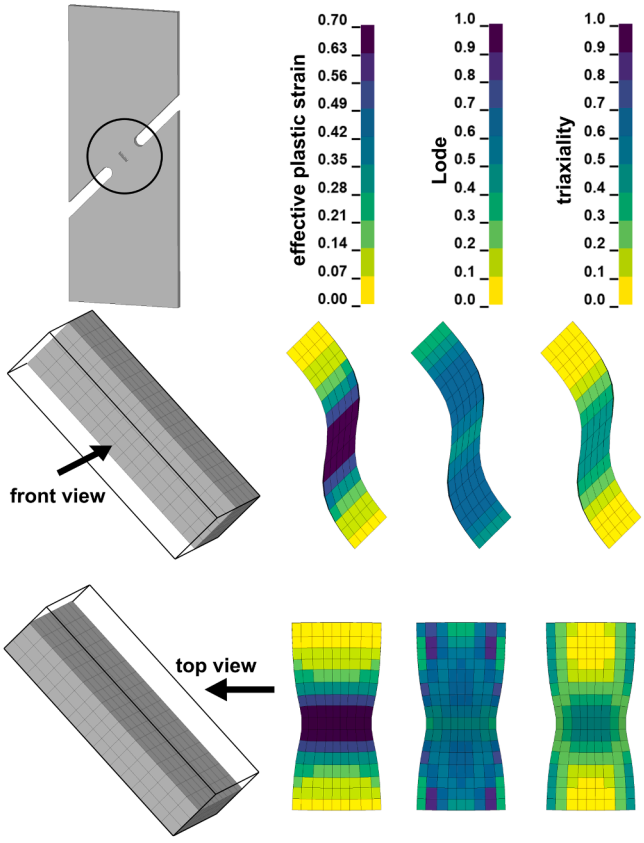


Fig. 23. Distribution of effective plastic strain, Lode value and triaxiality for shear test 45°.

shell element are almost identical, because the shear opening affects the overall behavior at the macroscopic scale more than the y_{CB}-displacement. It is expected that this would still be the case for a regularized shell simulation.

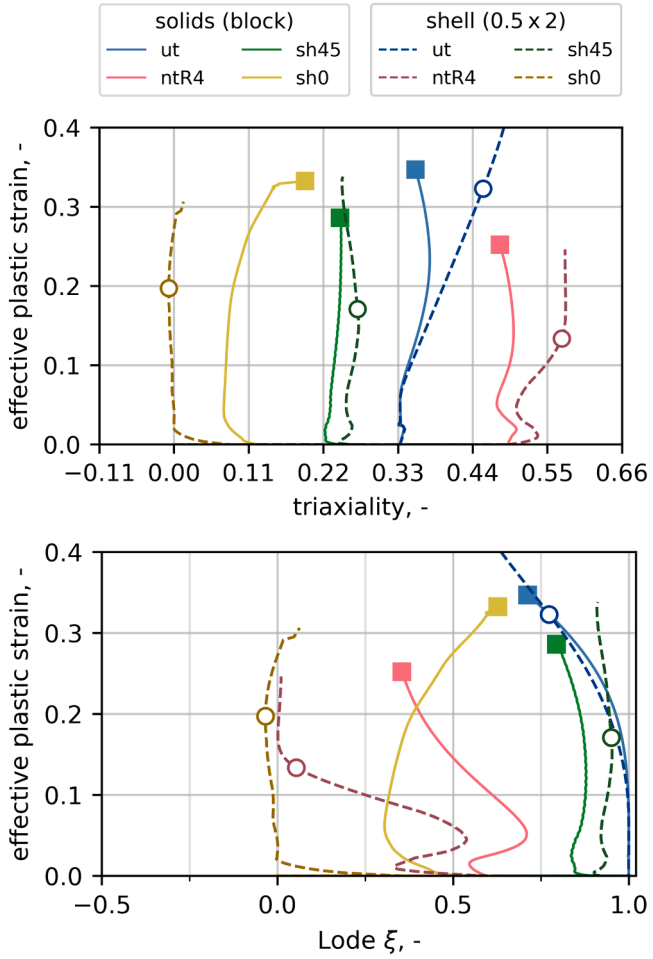


Fig. 24. Comparison of simulation with solids and shells (non-regularized) showing averaged values for a block of small solids and values for a single large shell element.

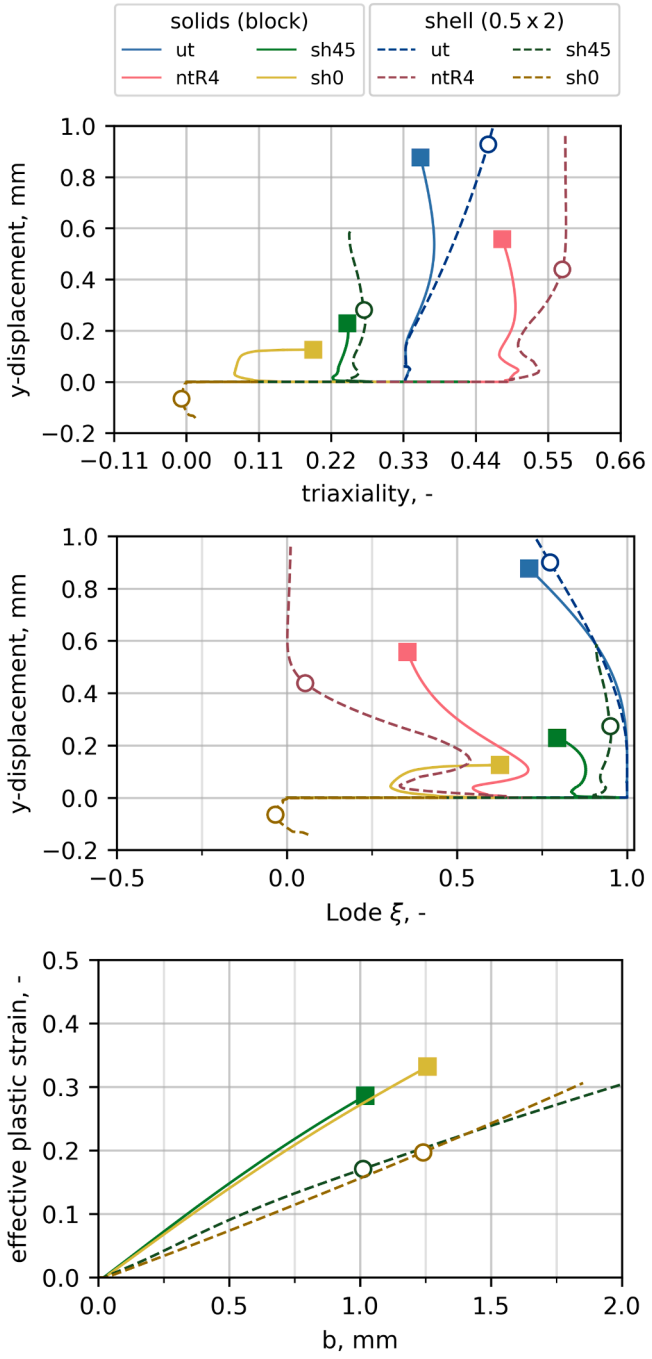


Fig. 25. Comparison of simulation with solids and shells (non-regularized) showing averaged y-displacement values and shear opening b for a block of small solids and values for a single large shell element.

3.5. *Example – spot welded specimen*

In this section, aspects of the proposed framework are tested on a problem that can be encountered in industrial application. The problem is application-oriented. However, no experimental data is available and the following analysis is purely a numerical demonstration. By using literature data, realistic target values for the simulation were selected by using the reported experimental data for a specimen geometry as described in Fig. 26.

When calibrating the finite element model of a spot weld with a softened heat-affected zone, the true stress-strain curve must first be scaled down, because the ring of shell elements is often approximately

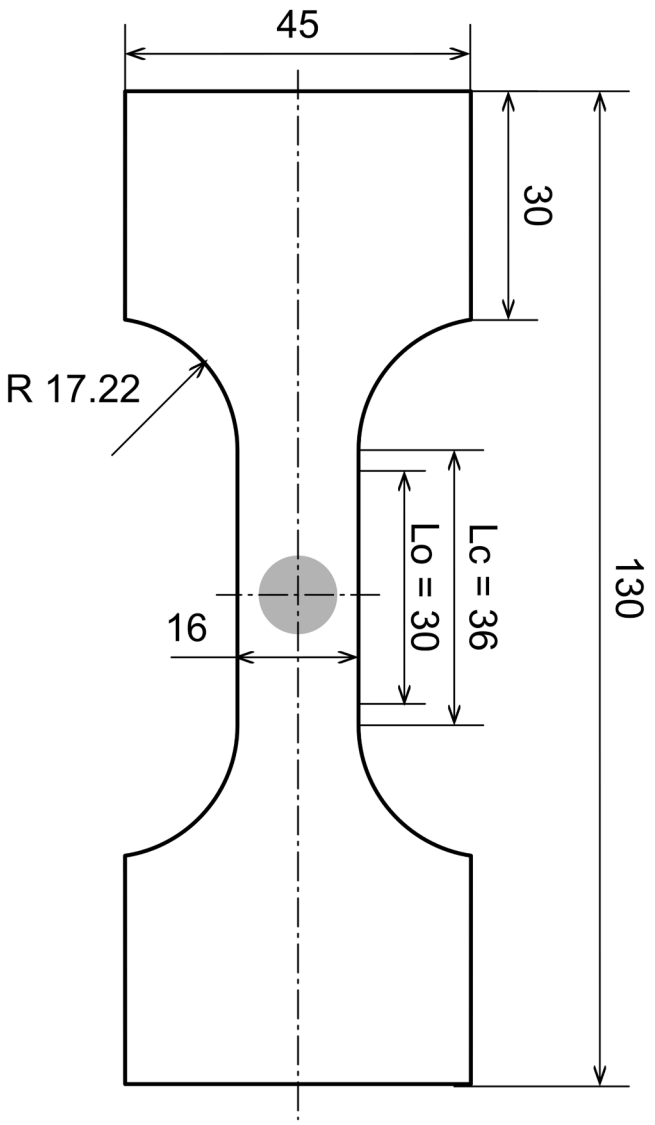


Fig. 26. Specimen geometry of a flat tensile test with a spot weld at the center.

Table 6
Characteristic lengths of the critical element for different discretizations.

	Standard calculation $\sqrt{A}$, mm	Projected length, mm
octagon	3.2	2.2
octagon, rotated	3.2	2.4
hexadecagon	2.2	2.3
hexadecagon, rotated	2.2	2.6

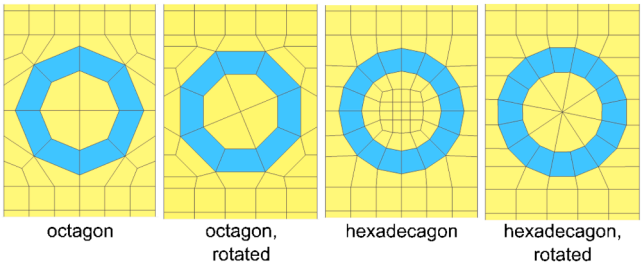


Fig. 27. Variations of mesh discretization for flat tensile test with spot weld.

three times thicker than the actual thickness of the softened heat-affected zone in order to keep the calculation time low. The scaling of the true stress-strain curve also accounts for the gradient of material properties present in the softened heat-affected zone. The material gradient also requires a scaling of the fracture locus. Because of the steep gradient of material properties, the edge at the transition represents a metallurgical notch and is prone to fracture initiation.

For the type of specimen used in this example, a global displacement to fracture between 0.5 mm and 1 mm can be expected. An arbitrary target value in this range of 0.8 mm was chosen. The scaling of the true stress-strain curve is omitted for this example.

In Table 6 the characteristic lengths of the critical elements for the different discretizations shown in Fig. 27 are listed. For the standard calculation of the characteristic length the octagon variations have a 45% larger characteristic length than the hexadecagon variations. To calculate the projected length, the length was calculated for the non-deformed mesh and the predicted crack opening direction was assumed to be the longitudinal direction for this example. The mean value of the two projected lengths of the diagonal corner nodes was calculated for this method (according to Fig. 4). The element shapes are equal for both octagon discretizations. However, the orientation of the element shapes is rotated between two discretizations. This results in two different sizes of characteristic length. The same is done for the hexadecagon discretizations. Due to the rotation, the characteristic length for the rotated octagon variation is 9% larger than that for the non-rotated octagon variation. For the variation hexadecagon rotated the characteristic length is 13% larger than that of its non-rotated counterpart. Overall, all characteristic lengths calculated from the projected lengths have similar sizes compared to the characteristic lengths calculated by the square root of the element area.

In Fig. 28 the longitudinal displacements u_y are plotted against the triaxiality for the critical element of each variation. The triaxiality during deformation remains constant for all variations and indicates a plane strain deformation with $\eta = \frac{1}{\sqrt{3}} \approx 0.577$. For simplicity the damage accumulation is not dependent on triaxiality and therefore when solving Equation (21), a damage value of $D = 1$ is reached when the displacement reaches the value of u_f. For a target value of global displacement 0.8 mm, the longitudinal displacement at failure was set to $u_f = 0.3mm$.

$$D = \int_0^u \frac{1}{u_f} du \tag{21}$$

The resulting displacement-force curves of the specimen deformations are shown in Fig. 28. The simulation was performed without stress coupling of damage. As discussed in Section 3.1, not all discretization errors can be compensated for by regularization. When the curvature of a geometric detail is not adequately captured by the discretization, it is not possible to recover this information by using regularization. Therefore, all variations predict slightly different values for the maximum force. The two rotated variants show an almost identical curve. Due to the rotation, the horizontal edges are exactly perpendicular to the direction of pull (see Fig. 27). Furthermore, one element lies exactly on the plane of symmetry and the load is not divided between two elements.

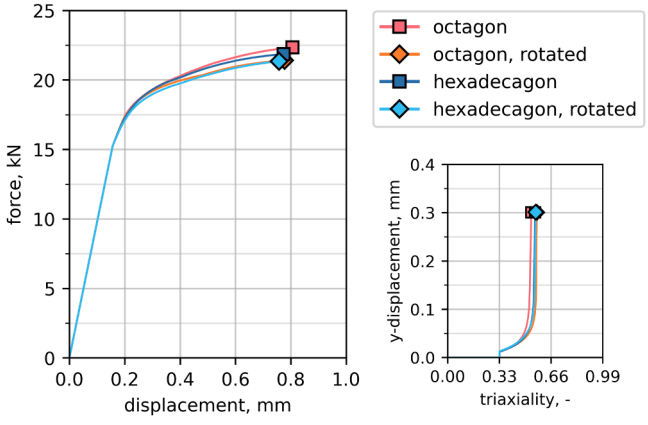


Fig. 28. Global force-displacement curve of flat tensile test specimens with spot weld and evolution of longitudinal displacement vs. triaxiality for the critical element in each variation.

This example demonstrates that the projected length is an adequate measure and leads to good agreement between different mesh discretization, even when the critical elements have significantly different sizes of area.

4. Conclusion

This study investigated the regularization of plane stress shell simulations of steel sheets using the crack band approach for different triaxialities and large shells with arbitrary element shapes and aspect ratios. Lower to mid-range triaxialities were covered by experimental tests of four specimen geometries. The experimental tests were simulated using solid and shell elements of various sizes. A direct comparison of solid simulations with shell elements was conducted to gain insights into the targeted deformation inside the localized zone.

The different aspect ratios for the solid elements revealed that the aspect ratios do not negatively affect the predicted fracture and softening behavior as long as the curvature of the localized zone is sufficiently resolved. This localized zone can be regarded as the crack band, which measured a height of approximately 2 mm.

For the shell simulations, square elements with an edge length of 0.5 mm led to a satisfactory agreement between simulation and experiment. Extending the element size along the width of the crack band to 0.75 mm did not negatively affect the results, and the crack band approach estimates the same characteristic length as for the square element, because only the projected length in the crack opening direction is of interest. When the element size is extended in crack band height direction, the characteristic length according to the crack band approach increases, which suggests the requirement of regularization. Indeed, extending the element in height leads to different results for the softening behavior and predicted fracture strain. Only the shear test 0° did not exhibit a change in softening when the element height was changed.

The simulations of solids and shells were directly compared by calculating averaged stress state values over a block of numerous solid elements representing a shell element of the same size and at the same position of the specimen. This comparison revealed that the lack of regularization requirement for the shear test 0° can most likely be attributed to the fact that no thickness reduction of the steel sheet occurs when this stress state is traversed. However, while the softening was not affected by the change in element size, the fracture strain was still affected, which leads to the assumption that the simple shear and coaxial stretch components need to be treated separately regarding regularization.

Both shear-dominated tests exhibited S-shaped bending of the localized zone within the block of solid elements. This effect is caused by the simple shear component. However, current frameworks for phenomenological damage models do not allow for the distinction between coaxial deformations and deformations involving simple shear.

The results regarding element size and aspect ratio can be used to improve the calibration methods for large shell elements. The targeted element size for these simulations is often large compared to the geometrical details of the specimens. By strategically placing elements with the targeted element size in the specimen center and shrinking the element edge length in the crack band width, a transition toward smaller notches can be modeled without compromising the calibration results.

Some aspects resulting from the developed guidelines were tested using flat tensile tests with a spot weld, which exhibits a softened heat-

affected zone. Although this test only covers one stress state, which does not have a simple shear component, it represents an actual problem found in the industry and suggests a possible refinement of existing regularization methods. In particular, the improved method of determining the characteristic length using the diagonal corner nodes and calculating the mean value of the projected lengths leads to improvements for arbitrarily shaped elements.

It is important to note that all solvers use different shell formulations and provide additional options to deal with the calculations of shell thickness, sharp value differences between element edge boundaries, and other drawbacks of shell elements. Therefore, the results obtained from shell simulations are often less generalizable than those obtained from solid elements. Therefore, a direct comparison of solid and shell simulations, as demonstrated in this study, can help in the development of better shell models.

Future studies should focus on using the presented guidelines of regularization combined with coupling stress to damage to improve the softening behavior of large shell elements. In addition, dealing with the regularization of stress states containing simple shear requires further investigation.

The findings of this study provide helpful guidelines for addressing mesh sensitivity in terms of aspect ratio, element size, and stress state for the calibration of shell elements in finite element analysis and the development of regularization methods. The results can help improve the shell simulations of steel sheets, which are relevant for automotive crash modeling.

CRediT authorship contribution statement

Lilia Schuster: Writing – original draft, Visualization, Methodology, Investigation, Formal analysis, Conceptualization. **Sebastian Münstermann:** Writing – review & editing, Supervision.

Declaration of Competing Interest

The authors declare that they have no known competing financial interests or personal relationships that could have appeared to influence the work reported in this paper.

Acknowledgements

The experimental work was conducted as part of the research project IFG 20998 N/P 1431. The research project IFG 20998 N/P 1431 “Development of methods for predicting the crash behavior of resistance spot welded 3-steel sheet joints” from the Research Association for Steel Application (FOSTA), Düsseldorf, was supported by the Federal Ministry of Economic Affairs and Climate Action the German Federation of Industrial Research Associations (AiF) as part of the program for promoting industrial cooperative research (IGF) on the basis of a decision by the German Bundestag. The authors thank the Fraunhofer-Institute for Mechanics of Materials for providing access to their high-performance computing cluster used for the finite element simulations.

Appendix

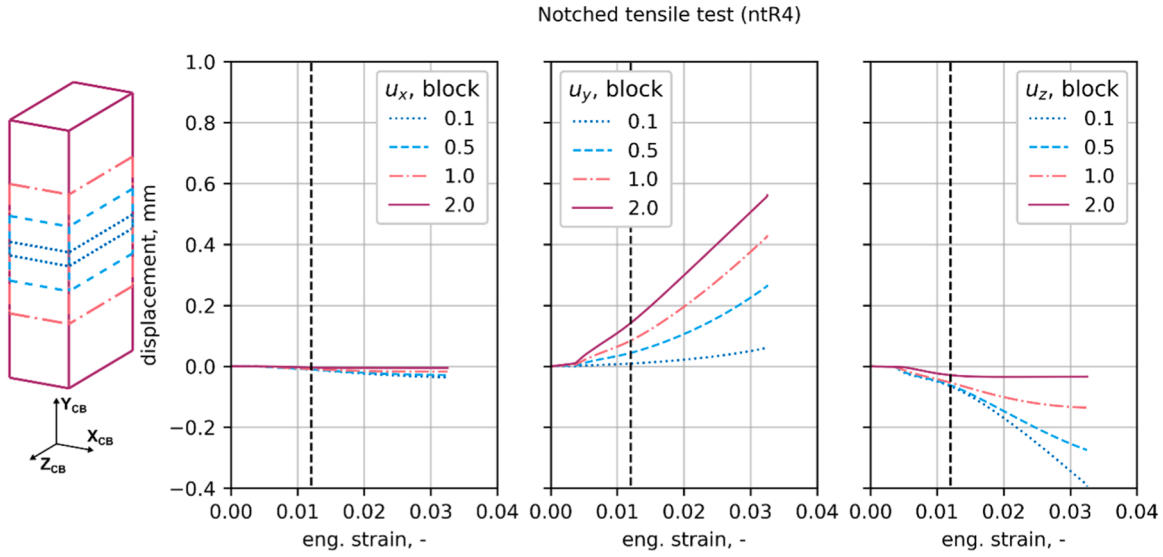


Fig. 29. Displacements of an element block in the center of the notched tensile test R4 with a section height of a) 0.1 mm, b) 0.5 mm, c) 1.0 mm, d) 2.0 mm

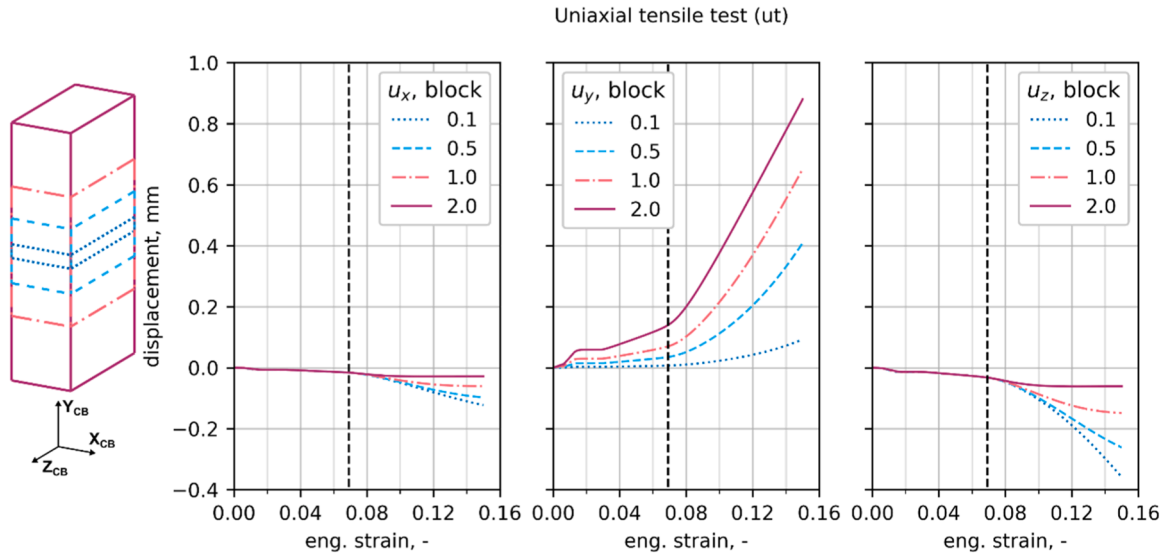


Fig. 30. Displacements of an element block in the center of the uniaxial tensile test with a section height of a) 0.1 mm, b) 0.5 mm, c) 1.0 mm, d) 2.0 mm

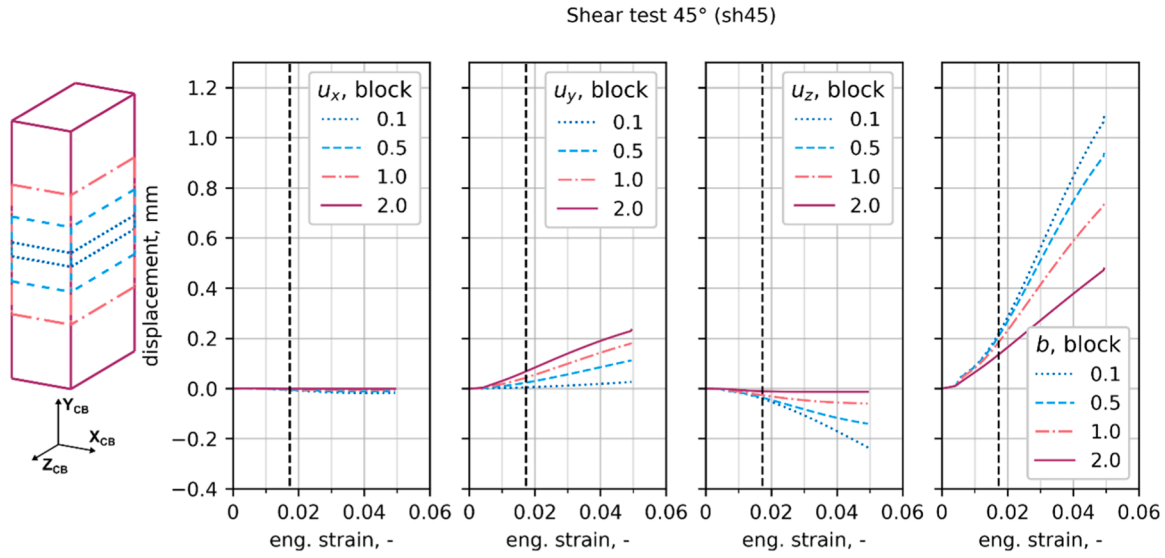


Fig. 31. Displacements of an element block in the center of shear test 45° with a section height of a) 0.1 mm, b) 0.5 mm, c) 1.0 mm, d) 2.0 mm

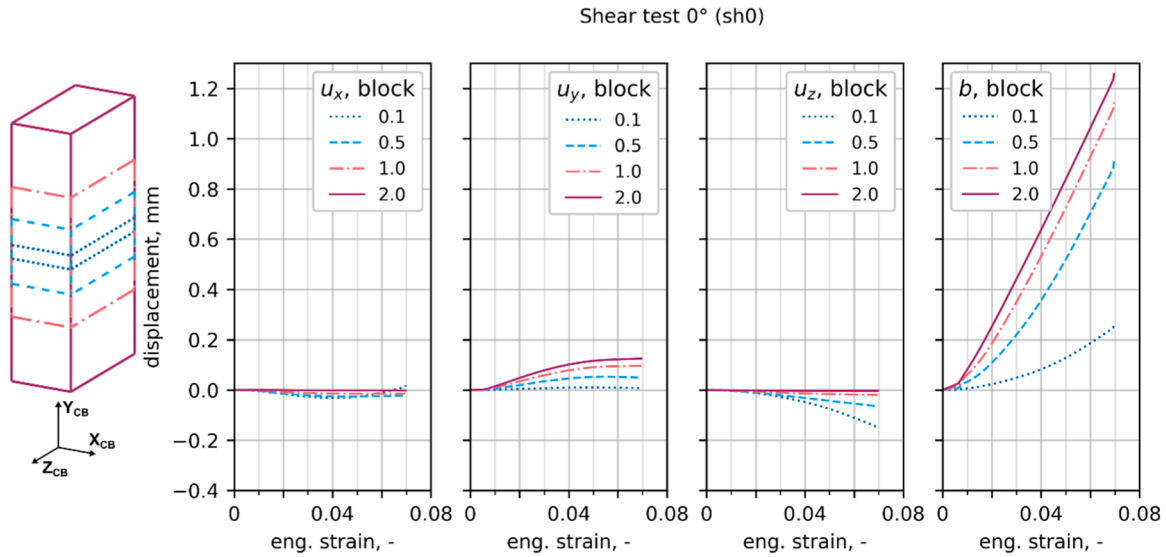


Fig. 32. Displacements of an element block in the center of the shear test 0° with a section height of a) 0.1 mm, b) 0.5 mm, c) 1.0 mm, d) 2.0 mm

Data availability

Data will be made available on request.

References

[1] A. Needleman, Some Issues in Cohesive Surface Modeling, Procedia IUTAM 10 (2014) 221–246, https://doi.org/10.1016/j.piutam.2014.01.020.

[2] R.G. Andersen, C.L. Felter, K.L. Nielsen, Micro-mechanics based cohesive zone modeling of full scale ductile plate tearing: From initiation to steady-state, Int. J. Solids Struct. 160 (2019) 265–275, https://doi.org/10.1016/j.ijsolstr.2018.10.027.

[3] A. Turon, C.G. Dávila, P.P. Camanho, J. Costa, An engineering solution for mesh size effects in the simulation of delamination using cohesive zone models, Eng. Fract. Mech. 74 (2007) 1665–1682, https://doi.org/10.1016/j.engfracmech.2006.08.025.

[4] K.L. Nielsen, J.W. Hutchinson, Cohesive traction–separation laws for tearing of ductile metal plates, Int. J. Impact Eng. 48 (2012) 15–23, https://doi.org/10.1016/j.ijimpeng.2011.02.009.

[5] P.B. Woelke, M.D. Shields, J.W. Hutchinson, Cohesive zone modeling and calibration for mode I tearing of large ductile plates, Eng. Fract. Mech. 147 (2015) 293–305, https://doi.org/10.1016/j.engfracmech.2015.03.015.

[6] I. Scheider, W. Brocks, Cohesive elements for thin-walled structures, Comput. Mater. Sci. 37 (2006) 101–109, https://doi.org/10.1016/j.commatsci.2005.12.042.

[7] Z.P. Bažant, B.H. Oh, Crack band theory for fracture of concrete, Mat. Constr. 16 (1983) 155–177, https://doi.org/10.1007/BF02486267.

[8] J. Červenka, V. Červenka, S. Laserna, On crack band model in finite element analysis of concrete fracture in engineering practice, Eng. Fract. Mech. 197 (2018) 27–47, https://doi.org/10.1016/j.engfracmech.2018.04.010.

[9] J. Červenka, Z.P. Bažant, M. Wierer, Equivalent localization element for crack band approach to mesh-sensitivity in microplane model, Numer. Meth Eng. 62 (2005) 700–726, https://doi.org/10.1002/nme.1216.

[10] B.C. Simonsen, R. Törnqvist, Experimental and numerical modelling of ductile crack propagation in large-scale shell structures, Mar. Struct. 17 (2004) 1–27, https://doi.org/10.1016/j.marstruc.2004.03.004.

[11] M. Storheim, H.S. Alsos, O.S. Hopperstad, J. Amdahl, A damage-based failure model for coarsely meshed shell structures, Int. J. Impact Eng. 83 (2015) 59–75, https://doi.org/10.1016/j.ijimpeng.2015.04.009.

[12] P.B. Woelke, N.N. Abboud, Modeling fracture in large scale shell structures, J. Mech. Phys. Solids 60 (2012) 2044–2063, https://doi.org/10.1016/j.jmps.2012.07.001.

[13] S. Schwarz, Ruhr-Universität Bochum, Effic. Approaches Regul. Damage Model. Var. Model. Numer. Treat. (2019), https://doi.org/10.13154/294-6554.

[14] M. Körgesaar, J. Romanoff, Influence of mesh size, stress triaxiality and damage induced softening on ductile fracture of large-scale shell structures, Mar. Struct. 38 (2014) 1–17, https://doi.org/10.1016/j.marstruc.2014.05.001.

[15] C.L. Walters, Framework for adjusting for both stress triaxiality and mesh size effect for failure of metals in shell structures, Int. J. Crashworthiness 19 (2014) 1–12, https://doi.org/10.1080/13588265.2013.825366.

[16] L. Wei, F. Qin, K. Cui, Prediction the stainless steel sheet fracture with mesh size effect for shell elements, Int. J. Solids Struct. 210–211 (2021) 35–48, https://doi.org/10.1016/j.ijsolstr.2020.11.013.

[17] M. Jirásek, M. Bauer, Numerical aspects of the crack band approach, Comput. & Struct. 110–111 (2012) 60–78, https://doi.org/10.1016/j.compstruc.2012.06.006.

[18] J. Oliver, A consistent characteristic length for smeared cracking models, Int. J. Numer. Methods Eng. 28 (1989) 461–474, https://doi.org/10.1002/nme.1620280214.

[19] J. Oliver, M. Caicedo, E. Roubin, A.E. Huespe, J.A. Hernández, Continuum approach to computational multiscale modeling of propagating fracture, Comput. Methods Appl. Mech. Eng. 294 (2015) 384–427, https://doi.org/10.1016/j.cma.2015.05.012.

[20] A. Hillerborg, The theoretical basis of a method to determine the fracture energyG F of concrete, Mater. Struct. 18 (1985) 291–296, https://doi.org/10.1007/BF02472919.

[21] C. Butcher, A. Abedini, On Phenomenological Failure Loci of Metals under Constant Stress States of Combined Tension and Shear: Issues of Coaxiality and Non-Uniqueness, Metals 9 (2019) 1052, https://doi.org/10.3390/met9101052.

[22] C. Butcher, A. Abedini, Shear confusion: Identification of the appropriate equivalent strain in simple shear using the logarithmic strain measure, Int. J. Mech. Sci. 134 (2017) 273–283, https://doi.org/10.1016/j.ijmecsci.2017.10.005.

[23] L. Schuster, S. Münstermann, Identifying simple shear in plane stress states, Int. J. Fract. 249 (2025) 43, https://doi.org/10.1007/s10704-025-00856-0.

[24] L. Schuster, V. Schulze, S. Münstermann, Ambiguities in Characterizing Stress States Involving Simple Shear, J. Phys Conf. Ser. 3104 (2025) 012048, https://doi.org/10.1088/1742-6596/3104/1/012048.

[25] S. Burget, Modellier. Des. Verformungs- und Versagensverhaltens Punkt-.-. ßTer. Mischverbindungen Zwischen mikrolegierten und Press. ärteten Stählen. Karlsr. Inst. Technol. (KIT (2015).

[26] T.K. Eller, L. Greve, M. Andres, M. Medricky, H.J.M. Geijselaers, V.T. Meinders, A. H. van den Boogaard, Plasticity and fracture modeling of the heat-affected zone in resistance spot welded tailor hardened boron steel, J. Mater. Process. Technol. 234 (2016) 309–322, https://doi.org/10.1016/j.jmatprotec.2016.03.026.

[27] O. Sherepenko, S. Jüttner, Transient softening at the fusion boundary in resistance spot welded ultra-high strengths steel 22MnB5 and its impact on fracture processes, Weld. World 63 (2019) 151–159, https://doi.org/10.1007/s40194-018-0633-3.

[28] Schuster L., Münstermann S. Characterization of Material Behavior Under Combined Simple Shear and Tension. Proceedings of the 15th International Conference on the Technology of Plasticity, in production.

[29] L. Schuster, V. Olfert, O. Sherepenko, C. Fehrenbach, S. Song, D. Hein, G. Meschut, E. Biro, S. Münstermann, Influences of Weld Nugget Shape and Material Gradient on the Shear Strength of Resistance Spot-Welded Joints, Steel Res. Int. 95 (2024) 2300530, https://doi.org/10.1002/srin.202300530.

[30] D. Mohr, S.J. Marcadet, Micromechanically-motivated phenomenological Hosford–Coulomb model for predicting ductile fracture initiation at low stress

triaxialities, Int. J. Solids Struct. 67–68 (2015) 40–55, https://doi.org/10.1016/j.ijsolstr.2015.02.024.
[31] F. Neukamm, M. Feucht, A. Haufe, Considering Damage Hist. crashworthiness Simul. (2009).
[32] F. neukamm, M. Feucht, K. Roll, A. Haufe, Closing Const. Gap Form. Crash Simul. (2008).
[33] Z.P. Bažant, Asce F. SIZE EFFECT IN BLUNT FRACTURE: CONCRETE. ROCK, METAL, 2005.
[34] J. Červenka, Z.P. Bažant, M. Wierer, Equivalent localization element for crack band approach to mesh-sensitivity in microplane model, Int. J. Numer. Methods Eng. 62 (2005) 700–726, https://doi.org/10.1002/nme.1216.
[35] M. Jirásek, M. Bauer, Numerical aspects of the crack band approach, Comput. Struct. 110–111 (2012) 60–78, https://doi.org/10.1016/j.compstruc.2012.06.006.